Osaka University Knowledge Archive : OUKA

https://ir.library.osaka-u.ac.jp/

Osaka University

Coarse grained DEM simulation of non-spherical and poly-dispersed particles using Scaled-Up Particle (SUP) model

Kimiaki Washino [a,b,*], Ei L. Chan [a,b], Yukiko Nishida [b], Takuya Tsuji [a,b]

[a] Department of Mechanical Engineering, Osaka University, Suita, Osaka 565-0871, Japan
[b] DENSE Ltd., Osaka Kita-ku, Osaka 530-0001, Japan

GRAPHICAL ABSTRACT
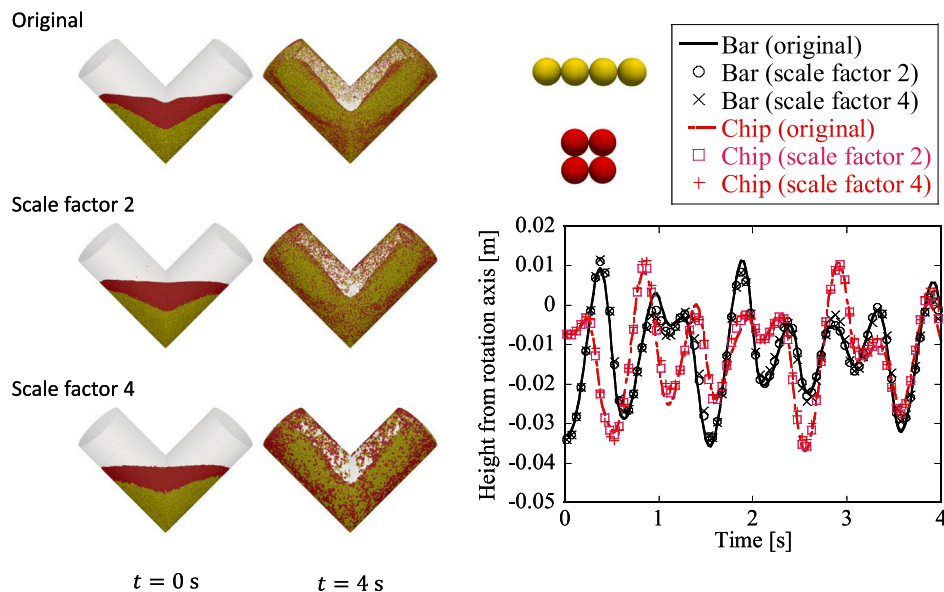
HIGHLIGHTS

- A novel coarse grain model is developed for the speed-up of DEM simulation.
- The scaling laws are based on the continuum assumption of an arbitrary flow.
- The scaling laws for non-spherical and poly-dispersed particles are derived.
- Good agreement between original and scaled-up particles are observed.
- The proposed model is universally applicable to any particle shape models.

ARTICLE INFO

ABSTRACT

In this work, the validity of the Scaled-Up Particle (SUP) model, which is a novel coarse grain model for Discrete Element Method (DEM), is examined to simulate a flow of non-spherical and poly-dispersed particles.

* Corresponding author at: Department of Mechanical Engineering, Osaka University, Suita, Osaka 565-0871, Japan.
  E-mail address: washino.k@mech.eng.osaka-u.ac.jp (K. Washino).

The SUP model is based on the authors' previous work and the scaling law is derived from the continuum assumption of an arbitrary particles flow. We discuss that the model is applicable not only to spherical and mono-dispersed particles, as is the case tested in the previous work, but also to non-spherical and poly-dispersed particles. Simulations of various systems are performed such as compression of a particle bed, heap formation, high shear mixer, large scale rotary drum and V-mixer. It is shown that the results obtained from the SUP model are in both qualitative and quantitative agreement with those from the original particles as long as the resolution is sufficiently high.

1. Introduction

Various kinds of powders and particles can be found in nature or produced in industry, and they are stored, transported, mixed and/or separated in a wide range of engineering applications. Individual particle properties such as size, shape and surface energy can have a considerable impact on the way the particles interact with neighbouring particles and wall boundaries, which affects the bulk flow dynamics. However, particle level interactions are extremely complex and challenging to be observed by experiment, and our knowledge today is still limited. Therefore, the design of equipment and process conditions are often determined empirically which is inefficient and requires numerous trial-and-errors.

Numerical simulation can be a powerful alternative tool to understand the underlying physics to achieve better process control, optimisation and troubleshooting. Discrete Element Method (DEM) [1] has become a particularly popular choice of simulating particulate flows where the movement of particles is carefully tracked in a Lagrangian manner. One of the main advantages of DEM over a Eulerian model is that the individual particle properties and the inter-particle interactions can be directly considered.

In many studies in the literature (e.g., [2,3]), spherical particles are used in DEM because of (a) fast contact detection, (b) simple form of the rotational equation to solve, and (c) easy implementation in a numerical code. However, most of the real-life particles are not spherical but have complex shapes. Rolling resistance [4,5] is sometimes utilised to artificially take into account particle non-sphericity while using spherical particles. Although this is an easy and convenient method, it is still unclear how much the rolling resistance alone can mimic various physical effects caused by particle shape such as particle inter-locking [6]. To the best of the authors' knowledge, there is no rule of thumb to determine the type and magnitude of rolling resistance to properly represent the high non-sphericity of particles.

Several models are already proposed and used in the literature to directly represent the non-sphericity of particles in DEM. A good review can be found in [7]. One of the most commonly used models is the multisphere model that uses multiple sub-spheres rigidly clumped together to represent one non-spherical particle [8–12]. In this way, the particle contact can be detected using the same algorithm for spheres, and any shape, in theory, can be represented by changing the number, size and position of the sub-spheres. The drawbacks are (a) the computational cost increases rapidly as the number of sub-spheres increases and (b) the resultant particle surface has perceptible roughness in the scale of the sub-spheres. Another popular model to explicitly handle particle non-sphericity is the polyhedral model [13–15] where one particle consists of multiple facets. It can represent arbitrary particle shape even with sharp corners. However, very small facets are required to properly represent a particle surface with high curvature, which can increase the computational cost enormously. An alternative approach is to implicitly capture particle shape using a mathematical function. Particularly, the superquadric function, which is first introduced by Barr [16], has attracted much attention since it can describe a variety of non-spherical shapes commonly found in engineering applications such as ellipsoids, cuboids, disks and rods by changing only 5 parameters for size and blockiness [12,17,18]. Although it cannot represent arbitrary or irregular shape unlike the aforementioned two models, it can provide

smooth particle surface without employing small elements. However, the particle contact is usually detected in an iterative manner and may become a bottle neck when the particles have low curvature surfaces. In summary, all of these models have pros and cons, and a suitable one should be selected depending on the particle type used in the system of interest.

One of the major problems of DEM is the extremely high computational cost to track the movement of a large number of particles. Even with the recent advancement of computational power, it is still difficult or practically impossible to complete large-scale simulation within an acceptable period of time. Therefore, various methods have been proposed and used for simulation speed-up; GPU computing [19–21], domain decomposition [22,23], reduced particle stiffness [24–28], and coarse grain model [29–40]. Especially, the coarse grain model is becoming increasingly popular since it has a potential to shorten the simulation time by many orders of magnitude.

In the coarse grain model, the particle size is artificially "scaled-up" by l times while keeping the system size the same so that the total number of particles is reduced by l^3 and the time step interval is increased by l [41]. A good review for the current coarse grain models is provided by Di Renzo et al. [42]. The coarse grain models in the literature are largely classified into two categories in the authors' previous work [43]: a parameter scaling approach [30,33,38] and direct force scaling approach [29,31,34,37,44,45]. In the parameter scaling, the input parameters of the scaled-up particles are adjusted to achieve similarity to the original particle system. Although this approach is easy to use, the scaling law of each parameter is usually dependent on the formulation of the force model, and it might not be easy or not even possible to derive the scaling law if the formulation is complex. In the direct force scaling, on the other hand, the forces acting on the original particles are first estimated using the original particle parameters and variables and then directly scaled for the scaled-up particles to obtain similar bulk flow. This approach tends to give simpler scaling laws and is attracting attention.

Relatively recently, the authors proposed a novel coarse grain model with direct force scaling [41,43,46]. This is called Scaled-Up Particle (SUP) model in this paper. In the SUP model, all forces exerted on particles are categorised into inter-particle forces (e.g., contact force and liquid bridge force) and body forces (e.g., gravitational force and fluid force), and the scaling law for each category is derived based on the continuum assumption of an arbitrary particles flow. One distinct advantage of the SUP model is that it only requires two scaling laws, i.e., one for the inter-particle forces and the other for the body forces. In other words, the same scaling law can be used to any forces as long as the force category is the same. In contrast, other coarse grain models in the literature have to derive force-specific scaling laws. Extensive validation studies and comparisons with the conventional coarse grain model can be found in [41].

Most, if not all, of the coarse grain models in the literature are tested with spherical particles. As mentioned above, simulation of non-spherical particles is even more computer-intensive than that of spherical particles, and it is highly demanded in the engineering community to reduce the computational cost for practical applications. In the authors' previous work [41,43,46], the validity of the SUP model is only examined with spherical and mono-dispersed particles. In this work, it is explained that the non-sphericity and poly-dispersity of the particles do not affect the derivation of the scaling laws in the SUP

model. The model is then applied to simulate various systems such as compression of a particle bed, heap formation, high shear mixer, rotary drum and V-mixer to investigate its validity. In the validation studies, both the multisphere and superquadric models are employed to represent the particle shape although any shape model can be used in theory. LIGGGHTS [47] is used for the simulations, which is open-source and fully customisable.

2. Discrete element method

2.1. Governing equations

The translational and rotational equations of motion of Particle i interacting with adjacent Particle j is given by:

$$m_i \dot{\boldsymbol{v}}_i = \sum_j \boldsymbol{F}_{Cij} + \boldsymbol{F}_{Gi} \tag{1}$$

$$\dot{\boldsymbol{L}}_i = \sum_j \boldsymbol{M}_{Cij} \tag{2}$$

$$\boldsymbol{L}_i = \boldsymbol{I}_i \boldsymbol{\omega}_i \tag{3}$$

where m is the particle mass, $\boldsymbol{v}$ is the translational velocity, $\boldsymbol{F}_C$ is the contact force, $\boldsymbol{F}_G = m\boldsymbol{g}$ is the gravitational force, $\boldsymbol{L}$ is the angular momentum, $\boldsymbol{M}_C$ is the contact torque, $\boldsymbol{I}$ is the tensor of inertia, and $\boldsymbol{\omega}$ is the angular velocity. Note that both $\boldsymbol{I}$ and $\boldsymbol{\omega}$ are defined in the global (observer-fixed) reference frame.

The orientation of particle is described as the rotation of the coordinate vectors of the global reference frame, i.e. $\boldsymbol{e}_x = (1,0,0)^{\mathrm{T}}$, $\boldsymbol{e}_y = (0,1,0)^{\mathrm{T}}$ and $\boldsymbol{e}_z = (0,0,1)^{\mathrm{T}}$, to the coordinate vectors of the local (body-fixed) reference frame, $\tilde{\boldsymbol{e}}_x$, $\tilde{\boldsymbol{e}}_y$ and $\tilde{\boldsymbol{e}}_z$. The rotation is tracked using the quaternion [48], $\boldsymbol{q}$, which is defined as:

$$\boldsymbol{q} = (q_0, q_1, q_2, q_3)^{\mathrm{T}} \tag{4}$$

The rotation matrix, $\boldsymbol{R}$, can then be constructed as:

$$\boldsymbol{R} = \begin{pmatrix} 1 - 2(q_2^2 + q_3^2) & 2(q_1 q_2 - q_0 q_3) & 2(q_1 q_3 + q_0 q_2) \\ 2(q_1 q_2 + q_0 q_3) & 1 - 2(q_1^2 + q_3^2) & 2(q_2 q_3 - q_0 q_1) \\ 2(q_1 q_3 - q_0 q_2) & 2(q_2 q_3 + q_0 q_1) & 1 - 2(q_1^2 + q_2^2) \end{pmatrix} \tag{5}$$

By definition, $\tilde{\boldsymbol{e}}_x = \boldsymbol{R}\boldsymbol{e}_x$, $\tilde{\boldsymbol{e}}_y = \boldsymbol{R}\boldsymbol{e}_y$ and $\tilde{\boldsymbol{e}}_z = \boldsymbol{R}\boldsymbol{e}_z$. The evolution of the quaternion of Particle i is governed by the following equation:

$$\dot{\boldsymbol{q}}_i = \frac{1}{2} \boldsymbol{q}_i \circ \tilde{\boldsymbol{\omega}}_i \tag{6}$$

where the operation $\circ$ is the quaternion multiplication [48], and $\tilde{\boldsymbol{\omega}} = \boldsymbol{R}^{-1}\boldsymbol{\omega}$ is the angular velocity in the local reference frame.

2.2. Contact force

In this work, an adhesive contact model based on the JKR theory [49] is used. The normal and tangential contact forces are given by:

$$\boldsymbol{F}_{Cn} = -\left(\frac{4E^*}{3r^*} a^3 - 4\sqrt{\pi\gamma E^* a^3} + \eta_n \boldsymbol{v}_{rel} \cdot \boldsymbol{n} \right) \boldsymbol{n} \tag{7}$$

$$\boldsymbol{F}_{Ct} = -\min[8G^* \sqrt{r^* \delta_n} \delta_t + \eta_t v_s, \mu_s F_N] \boldsymbol{t} \tag{8}$$

where a is the contact radius, γ is the surface energy, η is the damping coefficient, $\boldsymbol{v}_{rel}$ is the relative velocity, $\boldsymbol{n}$ is the unit normal vector, δ is the particle deformation (overlap), v_s is the magnitude of the relative tangential velocity at the contact surface, μ_s is the sliding friction coefficient, F_N is the normal load during sliding, and $\boldsymbol{t}$ is the unit tangent vector. The subscripts $_n$ and $_t$ indicate the normal and tangential directions, respectively. The reduced quantities indicated with the superscript * are defined as:

$$\frac{1}{r^*} = \frac{1}{r_i} + \frac{1}{r_j} \tag{9}$$

$$\frac{1}{E^*} = \frac{1 - v_i^2}{E_i} + \frac{1 - v_j^2}{E_j} \tag{10}$$

$$\frac{1}{G^*} = \frac{2(2 - v_i)(1 + v_i)}{E_i} + \frac{2(2 - v_j)(1 + v_j)}{E_j} \tag{11}$$

where r is the particle radius, E is the Young's modulus, and v is the Poisson's ratio.

The contact radius is given as the solution of the following equation [50]:

$$a^4 - 2r^* \delta_n a^2 - \frac{4\pi\gamma r^{*2}}{E^*} a + r^{*2} \delta_n^2 = 0 \tag{12}$$

The damping coefficients in the normal and tangential directions are given as [2]:

$$\eta_n = -2\sqrt{\frac{5}{3}} \beta (m^* E^*)^{1/2} r^{*1/4} \delta_n^{1/4} \tag{13}$$

$$\eta_t = -4\sqrt{\frac{5}{3}} \beta (m^* G^*)^{1/2} r^{*1/4} \delta_n^{1/4} \tag{14}$$

$$\frac{1}{m^*} = \frac{1}{m_i} + \frac{1}{m_j} \tag{15}$$

where β is a function of the restitution coefficient, e, and given as:

$$\beta = \frac{\ln(e)}{\sqrt{\ln^2(e) + \pi^2}} \tag{16}$$

F_N can be evaluated as [51,52]:

$$F_N = \left| 4\left(\frac{a}{a_0}\right)^3 - 4\left(\frac{a}{a_0}\right)^{3/2} + 2 \right| F_{po} \tag{17}$$

where F_{po} is the pull-off force and a_0 is the contact radius at the equilibrium condition, which are defined as:

$$F_{po} = 3\pi\gamma r^* \tag{18}$$

$$a_0 = \left(\frac{9\pi\gamma r^{*2}}{E^*} \right)^{1/3} \tag{19}$$

2.3. Superquadric model

In this work, two different shape models are used: superquadric and multisphere models. In the superquadric model, the particle shape is implicitly captured with the following function [16]:

$$f(\boldsymbol{X}) = \left(\left|\frac{X}{a}\right|^{n_2} + \left|\frac{Y}{b}\right|^{n_2} \right)^{n_1/n_2} + \left|\frac{Z}{c}\right|^{n_1} - 1 \tag{20}$$

$$\boldsymbol{X} = (X, Y, Z)^{\mathrm{T}} \tag{21}$$

where a, b, and c are the size parameters in each principal axis, and n_1 and n_2 are the blockiness parameters that control the edge sharpness as shown in Fig. 1. $\boldsymbol{X}$ is the position vector from the centre of the particle. The particle surface is defined as $f(\boldsymbol{X}) = 0$, and $f(\boldsymbol{X})$ takes a negative value inside the particle and a positive value outside the particle. The volume of the particle can be theoretically calculated as:

$$V_{sq} = 8abc \frac{\left[\Gamma\left(\frac{1}{n_2} + 1\right)\right]^2}{\Gamma\left(\frac{2}{n_2} + 1\right)} \frac{\Gamma\left(\frac{1}{n_1}\right)\Gamma\left(\frac{2}{n_1} + 1\right)}{n_1 \Gamma\left(\frac{3}{n_1} + 1\right)} \tag{22}$$

where Γ is the gamma function.

The contact detection is based on the iterative algorithm to find the midway point between particles [53]. In the contact force calculation, the particle radius is replaced with the volume equivalent sphere radius. Although employing the Gaussian curvature radius or the mean curvature radius at the contact point can give more accurate force evaluation, these radii may become very large depending on the particle shape and the time step interval may become excessively small for stable calculation. Employing the equivalent sphere radius can reasonably approximate the force–displacement curve according to the work by Podlozhnyuk et al. [53] without compromising the computational cost.
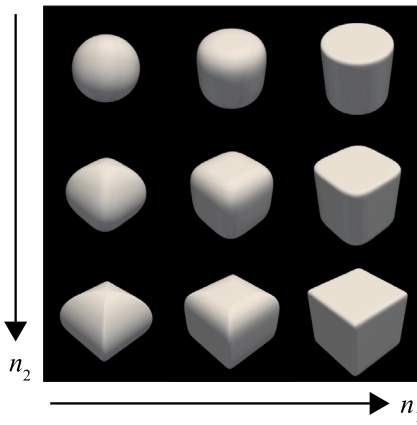
Fig. 1. Shape of superquadric particles with different blockiness parameters.
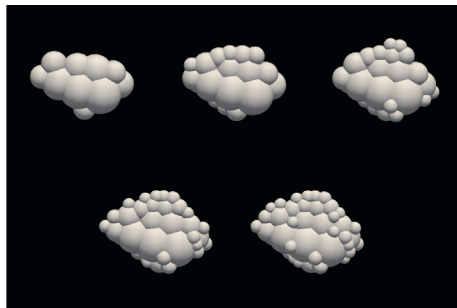

Fig. 2. Shape representation of a non-spherical particle with multisphere model using different number of sub-spheres.

2.4. Multisphere model

In the multisphere model, a single particle consists of multiple sub-spheres as shown in Fig. 2. The relative positions between the sub-spheres do not change with time. Arbitrary particle shape can be represented by changing the number, size and position of the sub-spheres. If needed, the sub-spheres can be overlapped with each other to increase the smoothness. The volume, centre of mass and inertia tensor are calculated using a Monte Carlo procedure.

The contact forces between the sub-spheres belonging to the neighbouring particles are computed based on the simple and fast contact detection algorithms used in the conventional DEM. The forces and torques acting on the sub-spheres are accumulated relative to the centre of mass of the particle [8].

3. Scaled-up particle (SUP) model

3.1. Scaled-up system

In the coarse grain model, the size of particles used in the simulation is artificially scaled-up while keeping the system size the same. In this work, the system with the original particle size is called "original system" whereas that with the increased particle size is called "scaled-up system". l is a scale factor and defined as:

$$l = (m_S/m_O)^{1/3} \tag{23}$$

where the subscripts $_O$ and $_S$ indicate the original and scaled-up systems, respectively. In the direct force scaling approach [43], the input parameters such as the particle density are unchanged when the particle size is increased. A novel coarse grain model is proposed in the authors' previous work [41,43,46], which is referred to as the Scaled-Up Particle (SUP) model in this work. The SUP model is based on the

Table 1
Relationships between original and scaled-up particle variables.

Variable	Relationship
Translational velocity [29]	$\boldsymbol{v}_O = \boldsymbol{v}_S$
Rotational velocity [29]	$\boldsymbol{\omega}_O = l\boldsymbol{\omega}_S$
Particle overlap [41]	$\delta_O = \delta_S/l$

continuum assumption of an arbitrary particles flow and maintains the same forces and torques acting on the control volumes (CVs) in the original and scaled-up systems (Fig. 3). The concept of the SUP model is briefly explained in the following sections.

3.2. Evaluation of original particle variables

The original particle variables, e.g., particle velocity and overlap, are required to estimate the forces and torques (e.g., contact forces and torques) acting on the original particles. Since the original particles are not explicitly simulated but represented by the scaled-up particles, the original particle variables need to be evaluated from those of the scaled-up particle. The relationships between the original and scaled-up particle variables are summarised in Table 1 [29,41]. The translational and rotational velocities are defined to keep the same total kinetic energy, and the relationship of the overlap is obtained from geometric similarity so that the same mass of particles are homogeneously distributed and accommodated in the CVs. More details on the evaluation of the original particle variables can be found in [41].

3.3. Scaling laws

It is assumed that the continuum assumption of the particles flow is valid, and a sufficient number of particles are accommodated in the CVs. In continuum mechanics, the forces acting on the CVs can be regarded as the rate of change of the momentum in the CVs [54]. The change of momentum is caused by the three mechanisms illustrated in Fig. 4: (a) the momentum exchanged between the neighbouring CVs with the movement of particles, (b) the momentum exchange caused by the inter-particle forces between particle pairs belonging to different CVs and (c) the momentum imparted to all particles in the CVs by body forces.

Since the relationships in Table 1 give the same particle velocity in the CVs between the original and scaled-up systems, no scaling is required for the momentum fluxes across CV faces related to the particle movement. On the other hand, the number of particle pairs interacting across the CV faces are reduced by l^2 in the scaled-up system. Hence the inter-particle forces such as the contact force should be scaled as follows to keep the same momentum exchange between the neighbouring CVs:

$$\boldsymbol{F}_{IS} = l^2 \boldsymbol{F}_{IO} \tag{24}$$

where $\boldsymbol{F}_I$ represents any inter-particle force. Finally, since the number of particles in the CVs are reduced by l^3 in the scaled-up system, the following scaling law should be used for the body forces such as the gravitational force:

$$\boldsymbol{F}_{BS} = l^3 \boldsymbol{F}_{BO} \tag{25}$$

where $\boldsymbol{F}_B$ represents any body force. The same concept can be applied to the torques and angular momentum, which leads to the following scaling for the inter-particle torques such as the contact torque:

$$\boldsymbol{M}_{IS} = l^2 \boldsymbol{M}_{IO} \tag{26}$$

where $\boldsymbol{M}_I$ represents any inter-particle torque.

One may notice that the resultant scaling laws above can be the same or similar to the conventional ones in literature in some (albeit limited) cases, for example, the fluid force scaling in [29] and normal
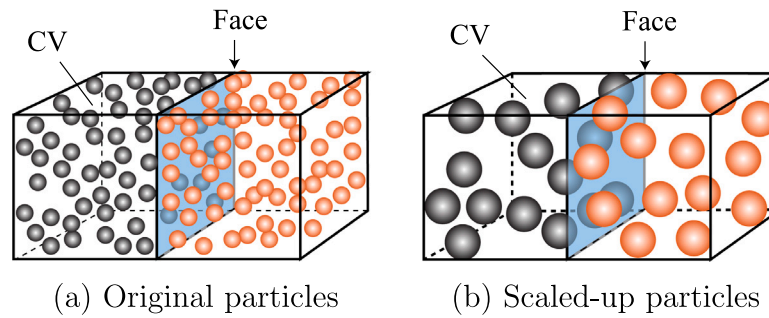
Fig. 3. Arbitrary particles flow and control volumes in (a) original and (b) scaled-up systems.
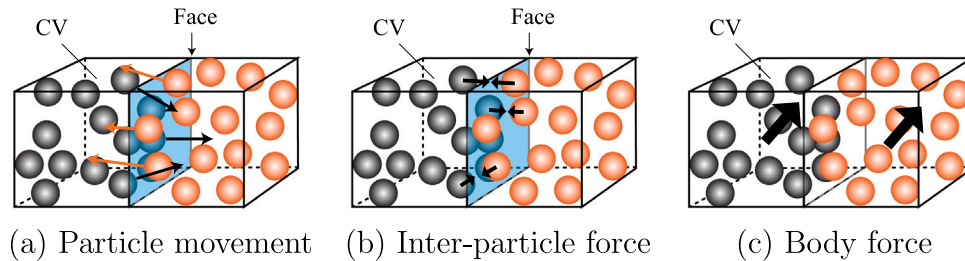

Fig. 4. Three mechanisms of momentum change in control volume due to (a) particle movement, (b) inter-particle force between particle pairs belonging to different CVs and (c) body force with spherical and mono-dispersed particles.
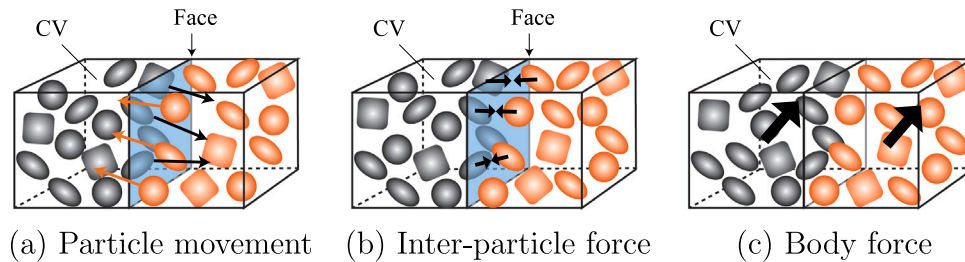

Fig. 5. Three mechanisms of momentum change in control volume due to (a) particle movement, (b) inter-particle force between particle pairs belonging to different CVs and (c) body force with non-spherical and poly-dispersed particles.

contact force scaling in [44]. However, it should be noted that there is a conceptual difference between the SUP and conventional models. In the conventional models, it is considered that one coarse grained particle "envelops" a group of original particles, and it is attempted to keep the particle level motion. In this way, the conventional models usually use force-specific scaling laws [29,31,44]. In the SUP model, on the other hand, the consistency of the translational and rotational motions is achieved in the control volume level (not in the particle level). One of the most distinct advantages of the SUP model is that it only requires two scaling laws: one for any inter-particle forces and torques and the other for any body forces. More details of the derivation of the scaling laws can be found in [46], and comparisons with other models in the literature can be found in [41].

3.4. Application to non-spherical and poly-dispersed particles

In all the validation studies presented in the authors' previous work [41,43,46], spherical and mono-dispersed particles are used for simplicity. However, the theories in Section 3.3 are generic, and the same scaling laws can be derived with non-spherical and poly-dispersed particles as shown in Fig. 5. It is also important to stress that any shape

models available for DEM can be used in principle, e.g., superquadric, multisphere and polyhedral models.

4. Results and discussion

In this section, simulations of non-spherical and poly-dispersed particles in various systems are presented to discuss the validity of the SUP model. In all simulations, the results obtained from the SUP model are compared with those from the original particles. Five different systems are employed: compression of a particle bed, heap formation, high shear mixer, large scale rotary drum and V-mixer.

4.1. Compression of particle bed

The SUP model is used to simulate compression of densely packed cohesionless particles, which can be regarded as a quasi-static and contact force dominant system. This is the simplest system tested in this work. Two different particle shapes are employed as shown in Fig. 6: (a) Shape I is a flat cube expressed with the superquadric model, and (b) Shape II is a dumbbell with the multisphere model. The size and shape parameters of the original particles are summarised in

Table 2
Size and shape parameters of original particles for bed compression simulation.

Shape	Particle type	Size parameters	Shape parameters
I	Superquadric flat cube	$a = 0.25$ mm $b = 0.25$ mm $c = 0.125$ mm	$n_1 = 4$ $n_2 = 4$
II	Multisphere dumbbell	$d_{sub} = 0.338$ mm	$N_{sub} = 2$ $L_{sub} = 0.338$ mm

Table 3
Common calculation conditions for bed compression simulation.

Property	Value
Particle density [kg/m^3]	2500
Young's modulus [MPa]	5
Poisson's ratio [–]	0.3
Restitution coefficient [–]	0.9
Sliding friction coefficient [–]	0.3
Surface energy [J/m^2]	0
Initial bed height [mm]	100

Table 4
Size and shape parameters of original particles for heap formation simulation.

Shape	Particle type	Size parameters	Shape parameters
A	Superquadric rod	$a = 0.328$ mm $b = 0.328$ mm $c = 0.657$ mm	$n_1 = 5$ $n_2 = 2$
B	Multisphere rod	See Table 5	
C	Sphere	$a = 0.459$ mm $b = 0.459$ mm $c = 0.459$ mm	$n_1 = 2$ $n_2 = 2$
D	Superquadric flat plate	$a = 0.63$ mm $b = 0.63$ mm $c = 0.158$ mm	$n_1 = 4$ $n_2 = 4$

Table 5
Positions and diameter of original sub-spheres of Shape B.

ID [–]	x [mm]	y [mm]	z [mm]	d_{sub} [mm]
1	0.000	0.000	−0.333	0.666
2	0.000	0.000	0.000	0.666
3	0.000	0.000	0.333	0.666
4	0.167	0.000	−0.500	0.333
5	0.083	0.144	−0.500	0.333
6	−0.083	0.144	−0.500	0.333
7	−0.167	0.000	−0.500	0.333
8	−0.083	−0.144	−0.500	0.333
9	0.083	−0.144	−0.500	0.333
10	0.167	0.000	0.500	0.333
11	0.083	0.144	0.500	0.333
12	−0.083	0.144	0.500	0.333
13	−0.167	0.000	0.500	0.333
14	−0.083	−0.144	0.500	0.333
15	0.083	−0.144	0.500	0.333

Table 6
Common calculation conditions for heap formation simulation.

Property	Value
Particle density [kg/m^3]	2000
Young's modulus [MPa]	5
Poisson's ratio [–]	0.3
Restitution coefficient [–]	0.3
Sliding friction coefficient [–]	0.5
Surface energy [J/m^2]	0.1
Feed rate [kg/s]	0.08
Feeding time [s]	4

Table 2. The diameter of the sub-spheres, d_{sub}, in the dumbbell (Shape II) is 0.338 mm, the number, N_{sub}, is 2, and the distance between the sub-sphere centroids, L_{sub}, is 0.338 mm, i.e., no overlap between the sub-spheres. Simulations using the original particles and scaled-up particles with $l = 2$ and 4 are performed as illustrated in Fig. 6c and 6d. Other common simulation conditions are listed in Table 3. The Young's modulus used is 5 MPa, which is rather low as compared to that of typical solid materials (such as glass). However, the main purpose of these simulations is to assess the capability of the SUP model, and the use of a low Young's modulus is not an issue as long as the same value is used in the original and scaled-up systems. The same applies to the simulations in the following sections.

The initial bed is prepared as follows. First, 0.037 kg of particles are randomly generated in the rectangular simulation domain with dimensions of $14 \times 14 \times 200$ mm^3. A plane wall is placed at the bottom and periodic boundaries are used in the horizontal directions. The sliding friction coefficient is set to a small value (0.05) at this stage to create a compact initial bed. The particles generated are settled by gravity and then removed if the height from the bottom is more than 100 mm. Finally, an upper wall is placed right above the bed surface.

The sliding friction coefficient is then set to 0.3 and the upper wall starts to move downwards to compress the bed with a constant speed of 5 mm/s while the bottom wall is fixed. Figs. 7 and 8 show the stress acting on the upper wall as a function of the strain with Shape I and II particles, respectively: (a) the results with the SUP model, i.e., the l^2 scaling for the contact force and torque, and (b) the results with the l^3 scaling. Note that the l^3 scaling is used for contact force in the literature [29], and it is shown here for comparison. It can be observed that the SUP model (Figs. 7a and 8a) can replicate the stress–strain curve well regardless of the scale factors and particle shapes. On the other hand, Figs. 7b and 8b show significant overestimation of the stress, which becomes even more pronounced as the scale factor increases.

4.2. Heap formation

Simulations of heap formation of cohesive particles as shown in Fig. 9 are presented in this section. Particles are continuously fed from a thin insertion region and settle by gravity to form a heap. The feeding is stopped at $t = 4$ s, and the simulation continues until a stable heap is formed. The simulations are performed using particles with different shapes as illustrated in Fig. 10: Shape A is a rod represented with the superquadric model, Shape B is a rod represented with the multisphere model, Shape C is a sphere and Shape D is a flat plate. The size and shape parameters of the original particles are listed in Table 4. These

parameters are chosen so that all shapes have approximately the same volume. The positions and diameter of the original sub-spheres of Shape B are provided in Table 5. Simulations using the original particles and scaled-up particles with $l = 2$ and 4 are performed. Other common simulation conditions are listed in Table 6.

The simulations are pseudo-2D with a domain size of $300 \times 30 \times 190$ mm^3. A flat wall is placed at the bottom boundary, and periodic boundaries are employed in the depth direction (i.e., the direction of the shortest edge of the simulation domain). The size of the particle insertion region is $12 \times 30 \times 30$ mm^3, and it is located at 175 mm from the bottom as illustrated by the solid line in Fig. 9. The resultant bulk volume of the heap, which can vary depending on the heap packing structure, is calculated from the image analysis of snapshots obtained from the simulations. The snapshots are binarised as shown in Fig. 11, and the projection area of the binarised image is multiplied by the depth of the simulation domain (i.e., 30 mm) to calculate the bulk volume. It is confirmed that the depth of the domain is sufficiently thin and there are negligible changes of the heap structure in this direction for all simulations.

Figs. 12 and 13 show the bulk volume of the heap as a function of time obtained from Shape A and Shape B particles (rods represented with the superquadric and multisphere models), respectively.
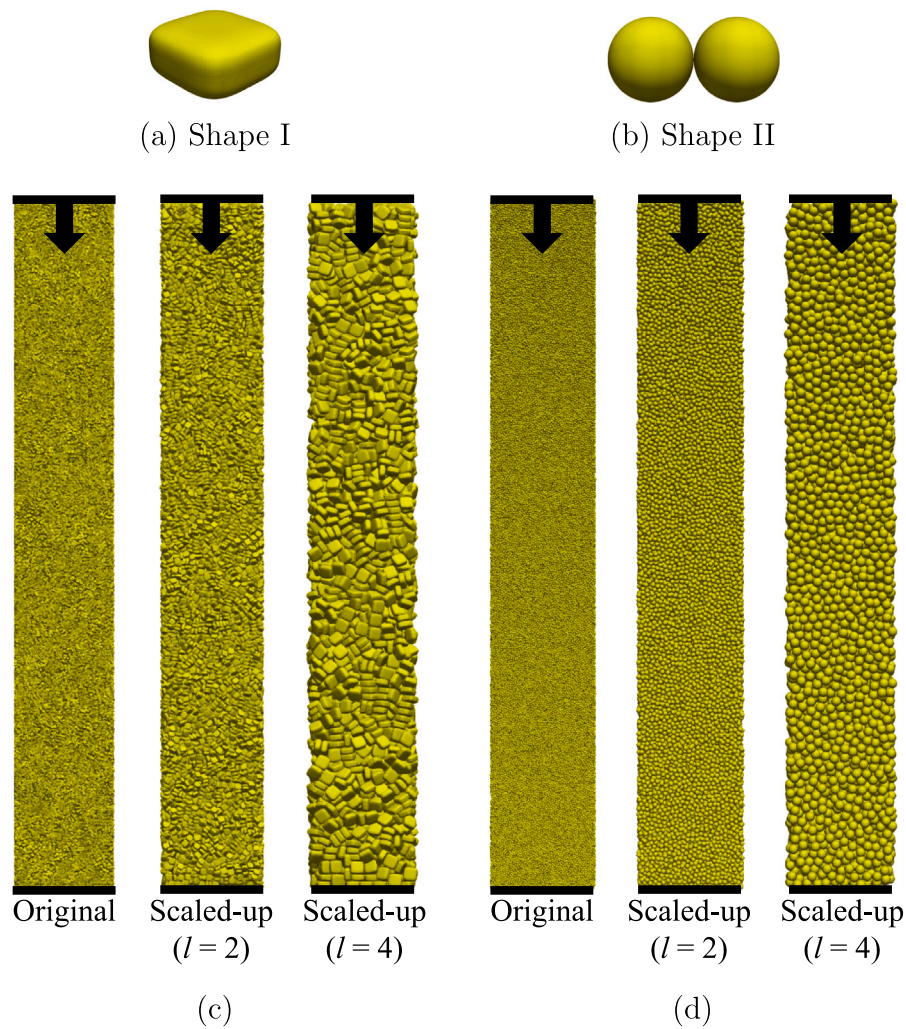
Fig. 6. Compression of packed particle bed with different shapes; (a) flat cube with superquadric model (Shape I), (b) dumbbell with multisphere model (Shape II), (c) initial bed with flat cubes and (d) initial bed with dumbbells.
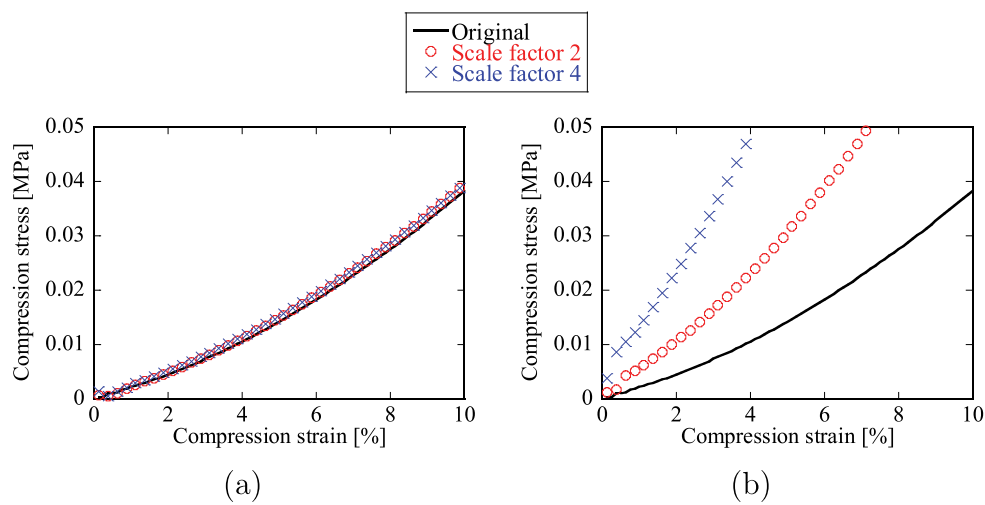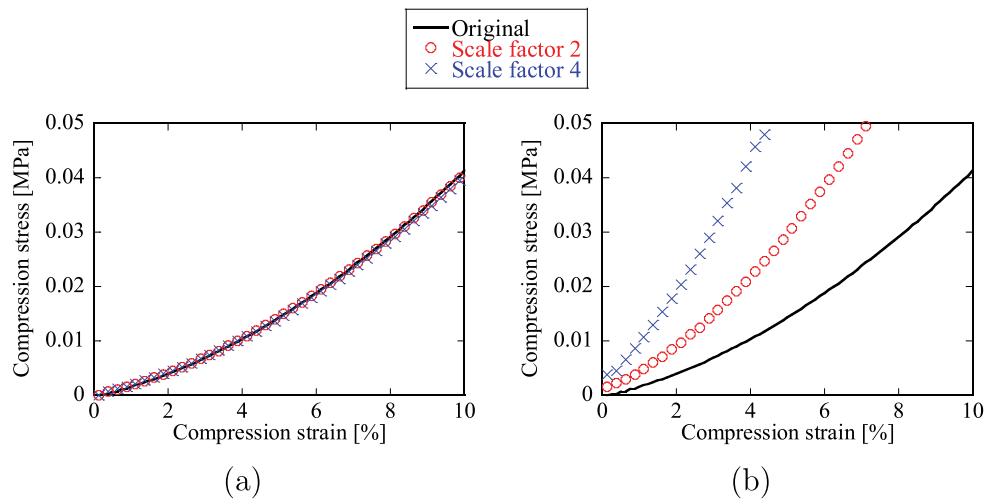

Fig. 7. Stress–strain curve during bed compression with Shape I particles (flat cube): (a) the SUP model and (b) l^3 scaling for contact force and torque.

The results with the l^3 scaling for the contact force and torque are also presented for comparison. In all cases, the bulk volume increases linearly with time while the particles are being fed, and then becomes constant soon after the feeding stops. In both Figs. 12b and 13b, the l^3 scaling notably overestimates the bulk volume, and the difference becomes more pronounced as the scale factor increases. This means

Fig. 8. Stress–strain curve during bed compression with Shape II particles (dumbbell): (a) the SUP model and (b) l^3 scaling for contact force and torque.

Fig. 9. Heap formation simulation at $t = 1, 2, 3, 4$ and 5 s from left to right. The particle insertion region is indicated with a solid line. The particle insertion is stopped at $t = 4$ s.
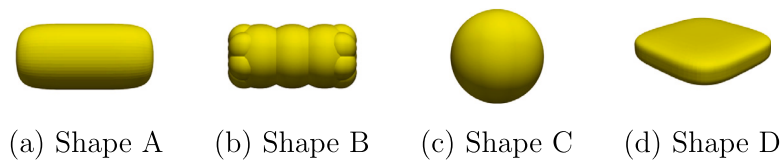
Fig. 10. Shape of particles used for heap formation; (a) Shape A is a rod represented with superquadric model, (b) Shape B is a rod represented with multisphere model, (c) Shape C is a sphere and (d) Shape D is a flat plate with superquadric model.
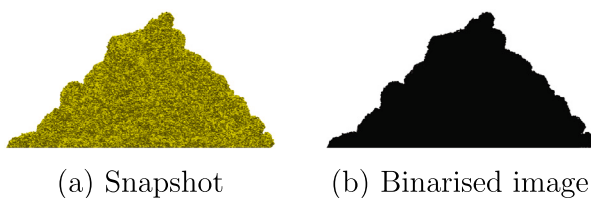
Fig. 11. Image analysis to calculate bulk volume of heap; (a) snapshot from simulation and (b) binarised image.

that the heap with l^3 scaling are more loosely packed than the original heap, which implies that the cohesion forces between the particles are overestimated. On the other hand, in both Figs. 12a and 13a, the results with the SUP model are almost identical to those with the original particles. Fig. 14 shows the superposition of Figs. 12a and 13a. It can be said that the rods represented with the superquadric and multi-sphere models are similar and can give comparable results. However, the final bulk volume in the original systems with the multisphere particles is approximately 4% larger than that with the superquadric particles. This may be because of the inherent roughness in the scale of the sub-spheres in the multisphere model, which could lead to

increased apparent friction and mechanical interlocking between the particles [55].

Fig. 15 shows the bulk volume of the heap as a function of time obtained from Shape A, Shape C and Shape D particles, where the shapes are all represented with the superquadric model. It can be observed that the bulk volume is strongly dependent on the particle shape. The heap of the spheres (Shape C) is the most compact, followed by the rod (Shape A), whilst the heap of the flat plates (Shape D) is the loosest. The bulk volume of Shape D in the final state is approximately 30% larger than that of Shape C in the original particle cases. It can also be seen that the SUP model successfully captures the shape dependency of the heap volume.

Fig. 16 shows the bulk volume of the heap as a function of time obtained from a 50:50 homogeneous mixture of Shape C and Shape D particles. It can be observed that the resultant bulk volume of this bi-dispersed system lies between those of the mono-dispersed systems of each shape, which may be reasonable intuitively. It is clear that the SUP model can properly predict the bulk volume of the original mixture. These results support the discussion in Section 3.4 that the SUP model can be applied not only to mono-dispersed but also poly-dispersed particles.
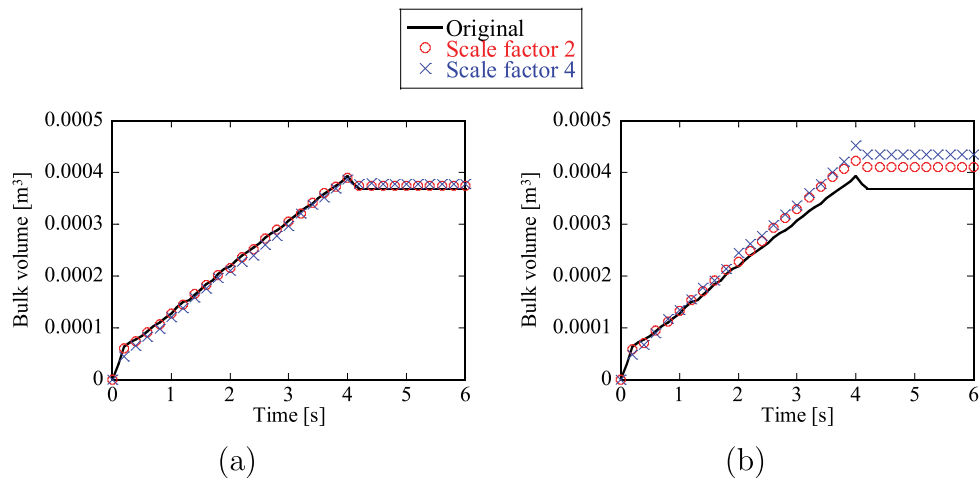
Fig. 12. Bulk volume of heap as a function of time with Shape A particles; (a) the SUP model and (b) l^3 scaling for contact force and torque.
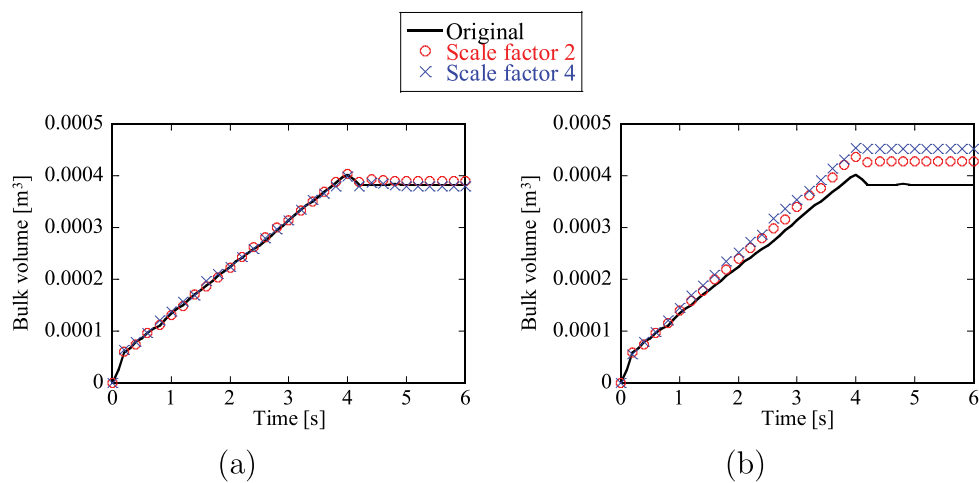

Fig. 13. Bulk volume of heap as a function of time with Shape B particles; (a) the SUP model and (b) l^3 scaling for contact force and torque.
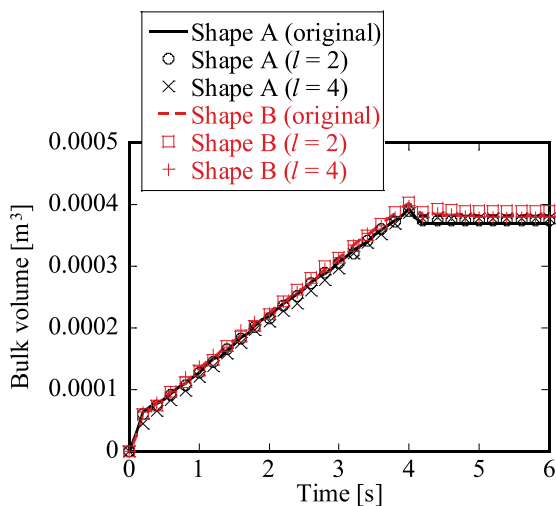

Fig. 14. Bulk volume of heap as a function of time with Shape A (superquadric rod) and Shape B (multisphere rod) particles.
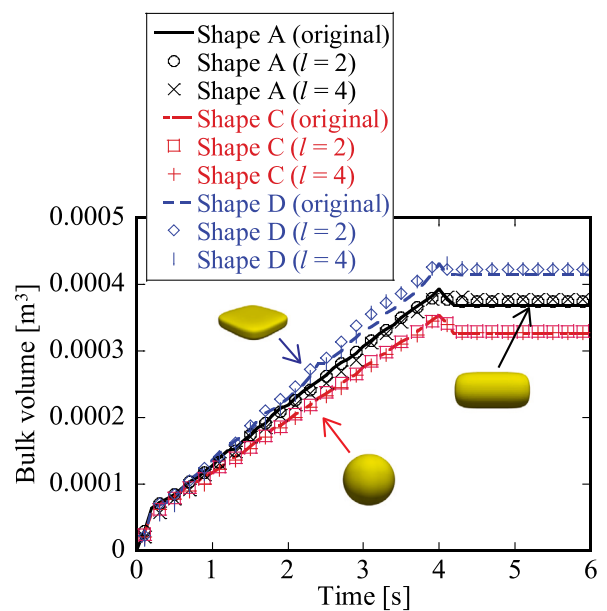

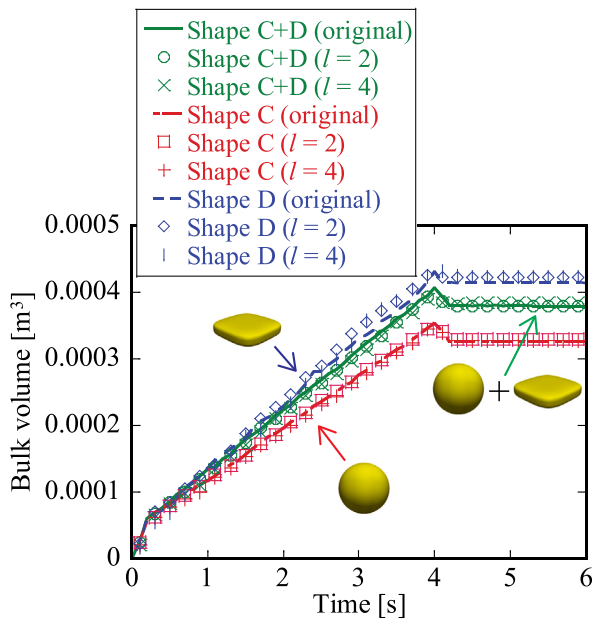**Fig. 15.** Bulk volume of heap as a function of time with Shape A, Shape C and Shape D particles.

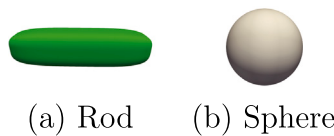**Fig. 16.** Bulk volume of heap as a function of time with the 50:50 mixture of Shape C and Shape D particles.

Fig. 17. Shape of particles used for high shear mixer simulation; (a) rod and (b) sphere particles represented with superquadric model.

4.3. High shear mixer

In Section 4.2, it is inferred that the SUP model can be used for poly-dispersed particles. We have performed simulations of a high shear mixer to further investigate the validity of the model for dynamic flows of cohesive non-spherical and poly-dispersed particles. As is the case in the authors' previous work [41,43], the mixer used is a scaled-down version of the 10L Roto Junior high shear granulator (Zanchetta Lucca). The inner diameter of the mixer is 84 mm and a 3-bladed impeller is mounted at the bottom. Superquadric rod particles as well as spherical particles as shown in Fig. 17 are employed where the size and shape parameters of the original particles are listed in Table 7. Both of the shapes have approximately the same volume. Three cases are considered as shown in Fig. 18: Case 1 with 100% superquadric rod particles, Case 2 with a 50:50 homogeneous mixture of the superquadric rod and spherical particles and Case 3 with 100% spherical particles. Other common simulation conditions are listed in Table 8. The particle–wall cohesion force is deactivated so that particles do not adhere to the casing wall and impeller, which could excessively reduce the amount of bulk moving particles available for analysis. Simulations with the original and scaled-up particles with $l = 2$ and 4 are carried out.

The 3×3 snapshots in Fig. 19 shows typical flow at steady state with Cases 1 (top row), Case 2 (middle row) and Case 3 (bottom row) in the (a) original system, (b) scaled-up system with $l = 2$ and (c) scaled-up system with $l = 4$. The results of the original systems (Fig. 19a) are first compared. A clear difference of the particle velocity can be seen among these cases. In Case 1 (100% rod particles), the colour of the particles near the casing wall is mostly red or orange indicating that the particles have large velocity, and the bed surface is rather rough. By mixing 50% of the spherical particles (Case 2), it can be observed that

Table 7
Size and shape parameters of original particles for high shear mixer simulation.

Shape	Size parameters	Shape parameters
Rod	$a = 0.136$ mm	$n_1 = 4$
	$b = 0.136$ mm	$n_2 = 4$
	$c = 0.545$ mm	
Sphere	$a = 0.25$ mm	$n_1 = 2$
	$b = 0.25$ mm	$n_2 = 2$
	$c = 0.25$ mm	

Table 8
Common calculation conditions for high shear mixer simulation.

Property	Value
Particle density [kg/m^3]	1000
Young's modulus [MPa]	5
Poisson's ratio [–]	0.3
Restitution coefficient [–]	0.1
Sliding friction coefficient [–]	0.3
Surface energy [J/m^2]	0.02
Total mass of particles [kg]	0.0458
Impeller rotation speed [rpm]	300

the particle velocity near the casing wall largely decreases, the volume of the bed also decreases and the bed surface becomes smoother. In Case 3 (100% spherical particles), the colour of the particles is mostly green or yellow except for the near-impeller region, the bed is more compacted and the particles flow smoothly. Qualitatively, the results obtained from the SUP model show a similar velocity field and bed structure of the original system.

Fig. 20 shows the probability density distributions of the particle velocity. In Case 1, a Gaussian-like distribution can be seen with relatively large peak velocity. In Case 2, the overall distribution is shifted to the left and a skewer peak can be observed. In addition, the distribution becomes less symmetric. In Case 3, the probability of smaller velocity increases, and the skew peak is further shifted to the left. Fig. 21 shows the peak velocity analysed from Fig. 20. The SUP model can reasonably predict the original difference of the peak velocity caused by the particle shape and poly-dispersity quantitatively.

4.4. Large scale rotary drum

Simulations of cohesionless and cohesive particles flows in a large rotary drum are presented in this section. The drum is 1 m in diameter, and the particle used is a superquadric flat plate with $a = 0.685$ mm, $b = 0.685$ mm, $c = 0.171$ mm, $n_1 = 4$ and $n_2 = 4$, i.e., the same shape as Shape D in Fig. 10 but slightly different in size. The equivalent sphere diameter of the particle is approximately 1 mm. Other common simulation conditions are listed in Table 9. The simulation is pseudo-2D with periodic boundaries in the depth direction of the drum, and the original particles as well as scaled-up particles with $l = 4$ and 8 are employed. The drum depth is adjusted so that the size ratio between the drum depth and equivalent sphere diameter is kept to 5. The total mass of the particles in the original system is 2.34 kg, and that of the scaled-up system increases proportionally to the scale factor since the drum depth increases accordingly. Three different values of surface energy are tested: $\gamma = 0$, 0.1 and 0.4 J/m^2.

Fig. 22 shows typical snapshots of the particles in the drum at steady-state with $\gamma = 0$ J/m^2 (top row), 0.1 J/m^2 (middle row) and 0.4 J/m^2 (bottom row) in the (a) original system, (b) scaled-up system with $l = 4$ and (c) scaled-up system with $l = 8$. A video is also provided as Supplementary material to show the movement of the particles. First, we discuss the flow pattern in the original systems (Fig. 22a). When $\gamma = 0$ J/m^2, i.e., no cohesion force, the flowability of the particles is good, and it shows a typical cascading motion [56,57] with a smooth profile of the bed surface. A clear and distinct band coloured by blue,
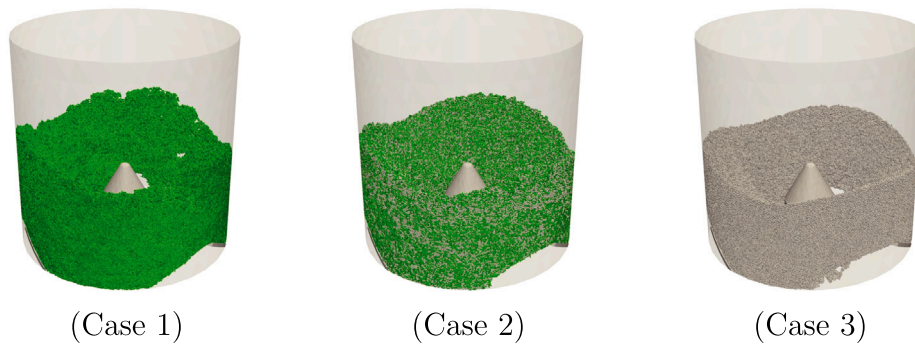
Fig. 18. Three cases for high shear mixer simulation; (Case 1) 100% rod particles, (Case 2) 50:50 mixture of rod and spherical particles and (Case 3) 100% spherical particles. The rod and spherical particles are coloured green and grey, respectively.
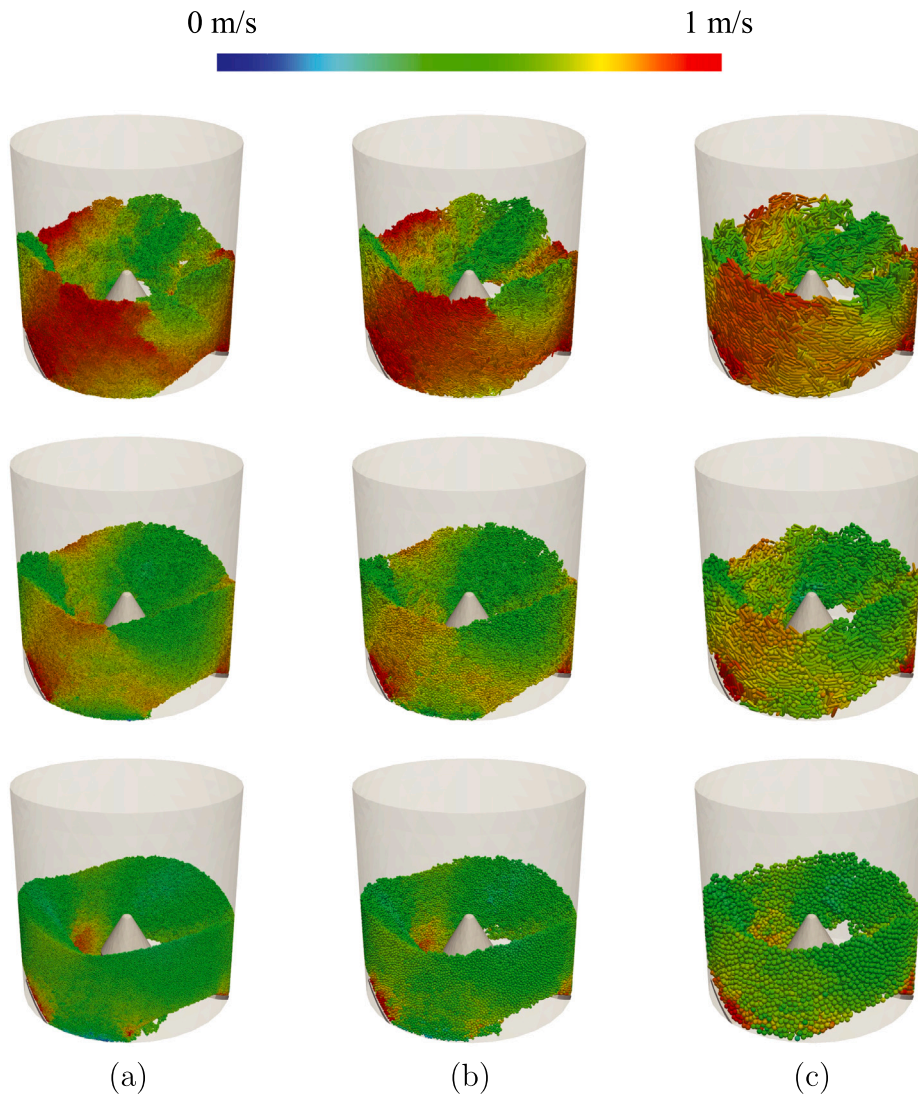

Fig. 19. Typical snapshots of particles in high shear mixer with Case 1 (top row), Case 2 (middle row) and Case 3 (bottom row); (a) original, (b) scaled-up ($l = 2$) and (c) scaled-up ($l = 4$) systems. The colour indicates the particle velocity.

above which the particles avalanche down, is formed all the way from the left to the right of the bed. When $\gamma = 0.1$ J/m^2, a similar flow pattern can be seen, but the particles in the avalanching region are more lumpy and the bed surface is less smooth. Finally, when $\gamma = 0.4$

J/m^2, the flow pattern changes drastically. A large chunk of particles is formed at the top of the bed due to the large cohesion force, and the blue band no longer reaches the right end of the bed. The chunk breaks into smaller lumps when falling by gravity, which then tumble down
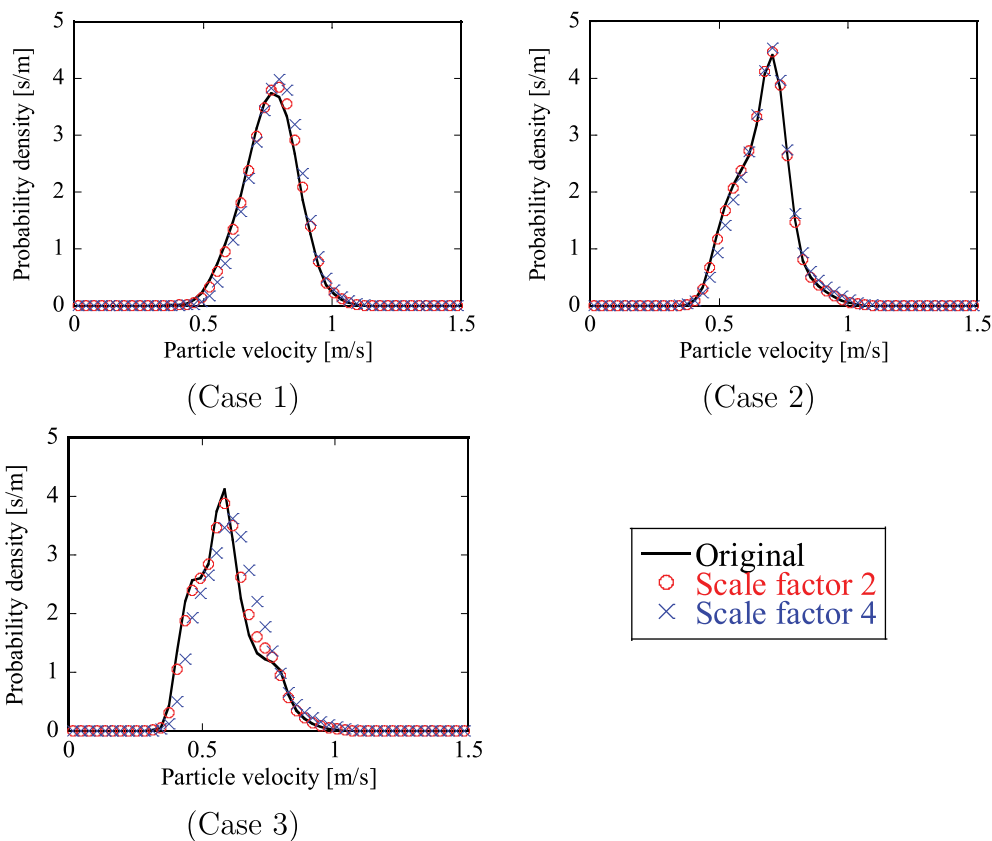
(Case 1)

(Case 2)

(Case 3)

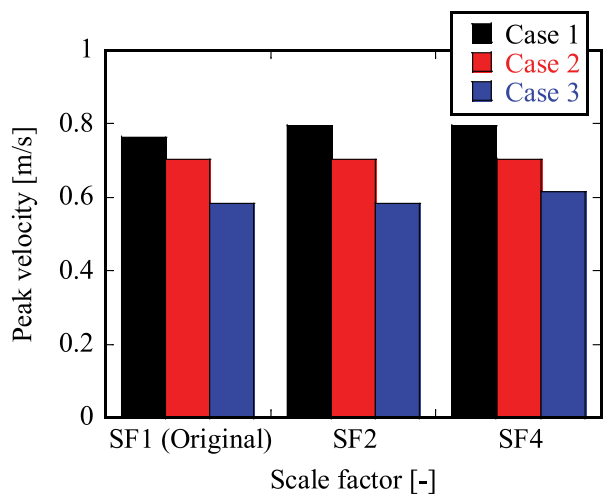**Fig. 20.** Probability density distribution of particle velocity in high shear mixer.

Fig. 21. Peak velocity of particles in high shear mixer.

the bed surface instead of avalanching. The scaled-up particles can qualitatively capture the flow patterns of the original systems described above although several discrepancies can be seen especially with $l = 8$, e.g., some particles are detached from the upper side of the drum wall when $\gamma = 0.1$ J/m^2, and the size of the lumps is relatively large when $\gamma = 0.4$ J/m^2. These discrepancies are caused by the lack of spacial resolution: the size of the scaled-up particle is too large to resolve the characteristic flow structure such as the particles attached on the wall

and the size of the lumps. In this sense, the size of a scaled-up particle is analogous to the cell size for Computational Fluid Dynamics (CFD). The scale factor should be determined from sensitivity analysis to ensure that the flow structure of interest can be reasonably resolved, just like one performs a mesh sensitivity study for CFD simulation. Note that this is a general limitation of the coarse grain models and not specific to the SUP model. Nevertheless, the overall flow patterns and structures can be reproduced even with the large scale factor, which can be useful in many engineering applications.

Fig. 23 shows the time averaged solid fraction in the drum over 1 s. The dashed lines and arrows indicate the dynamic angle of repose and the height at which the particles are detached from the drum wall, respectively. It can be seen that the dynamic angle of repose increases as the surface energy increases whilst the height at which the particles are detached decreases. In addition, the boundary of the bed surface becomes blur as the surface energy increases due to the formation of lumps. A qualitatively good agreement can be seen between the original and scaled-up systems. This reinforces the fact that the SUP model can well capture the sensitivity of the overall flow structures to the particle cohesiveness.

For more quantitative comparisons, the probability density distributions of the particle velocity with $\gamma = 0$, 0.1 and 0.4 J/m^2 are plotted in Fig. 24. Two distinct peaks can be observed when $\gamma = 0$ J/m^2. The first peak arises from the cascading motion. The second peak almost agrees with the drum wall velocity (0.785 m/s), which indicates that the particles near the wall are likely to be in a "solid-like" state that move rigidly with the wall. A similar bimodal velocity distribution can be seen with $\gamma = 0.1$ J/m^2, but the first peak is less pronounced because the cascading motion is retarded by the cohesion force. Finally, the first peak completely disappears when the surface energy increases to 0.4 J/m^2, and the flow pattern is changed drastically. The scaled-up
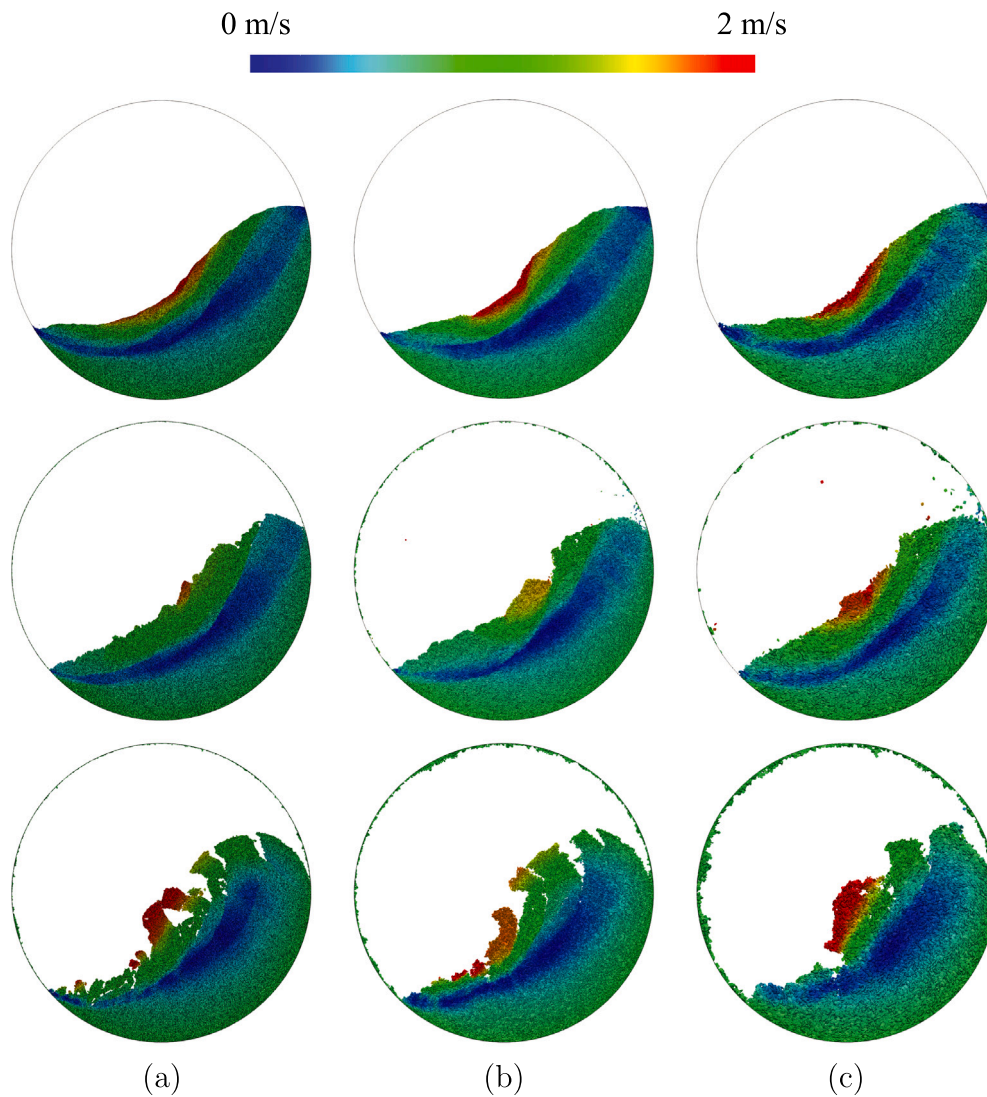
0 m/s

2 m/s

(a)

(b)

(c)

Fig. 22. Typical snapshots of particles in rotary drum with $\gamma = 0$ J/m² (top row), $\gamma = 0.1$ J/m² (middle row) and $\gamma = 0.4$ J/m² (bottom row); (a) original, (b) scaled-up ($l = 4$) and (c) scaled-up ($l = 8$) systems. The colour indicates the particle velocity.

particles can capture the overall velocity distributions of the original particles as well as the surface energy dependency of the flow pattern.

4.5. V-mixer

Finally, the SUP model is applied to simulate the flows of both cohesionless and cohesive particles in a V-mixer. This is the most complex system used in this work since the flow changes with time depending on the orientation of the mixer. The particles used are multisphere bars and chips as shown in Fig. 25, both of which consist of 4 identical sub-spheres with a diameter of 0.32 mm without overlap. The equivalent sphere diameter of these particles is 0.51 mm. The dimensions of the V-mixer are given in the work of Kuo et al. [58]: two cylinders with a diameter of 66 mm and height of 147 mm are slanted 45° in the opposite directions, clipped with the vertical axis at the tip and unified smoothly. The mixer rotates with 60 rpm with respect to the rotation axis located at 76 mm from the bottom of the mixer. The simulation conditions are listed in Table 10. Two different values of surface energy are tested: $\gamma = 0$ and 0.01 J/m². Simulations using the original particles and scaled-up particles with $l = 2$ and 4 are performed.

Table 9
Common calculation conditions for rotary drum simulation.

Property	Value
Size parameters a, b, c [mm]	0.685, 0.685, 0.171
Shape parameters n_1, n_2 [–]	4
Particle density [kg/m³]	2500
Young's modulus [MPa]	5
Poisson's ratio [–]	0.25
Restitution coefficient [–]	0.9
Sliding friction coefficient [–]	0.3
Surface energy [J/m²]	$0 \sim 0.4$
Drum rotation speed [rpm]	15

The initial particle bed is prepared as follows. First, the bar particles are continuously fed from a flat insertion region located at 80 mm from the mixer bottom until it reaches 0.2 kg. After the bar particles are settled by gravity, 0.2 kg of the chip particles are fed from the same insertion region. In this way, the bar and chip particles in the initial bed are almost completely segregated. During the initial packing stage, the mixer is stationary and the surface energy is set to 0 J/m² to avoid the particles sticking on the wall.
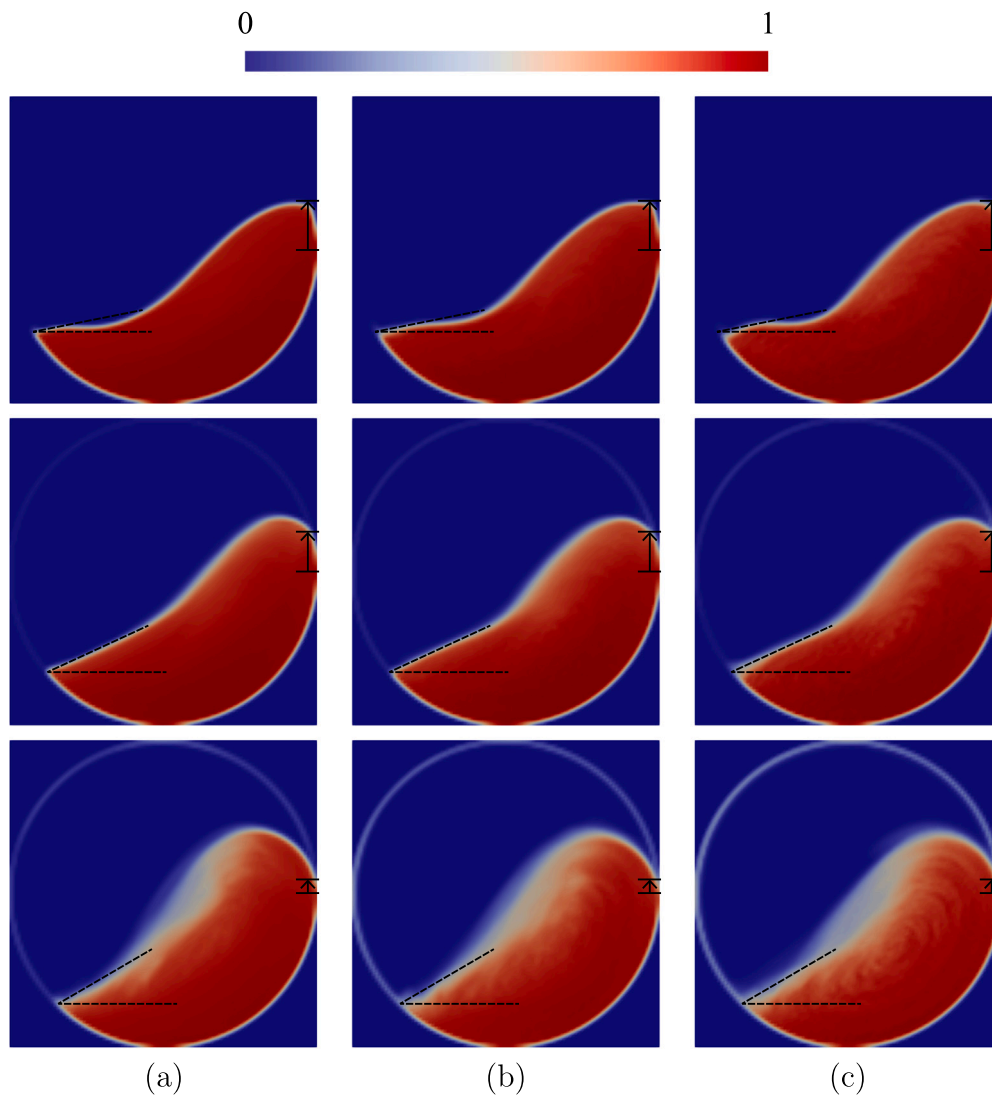
Fig. 23. Time averaged solid fraction in rotary drum with $\gamma = 0$ J/m^2 (top row), $\gamma = 0.1$ J/m^2 (middle row) and $\gamma = 0.4$ J/m^2 (bottom row); (a) original, (b) scaled-up ($l = 4$) and (c) scaled-up ($l = 8$) systems. The dashed lines and arrows indicate the dynamic angle of repose and the height at which the particles are detached from the wall, respectively.

Table 10
Calculation conditions for V-mixer simulation.

Property	Value
Particle density [kg/m^3]	2500
Young's modulus [MPa]	5
Poisson's ratio [–]	0.25
Restitution coefficient [–]	0.9
Sliding friction coefficient [–]	0.3
Surface energy [J/m^2]	0, 0.01
Total mass of particles [kg]	0.4
Mixer rotation speed [rpm]	60

Figs. 26 and 27 show the front view of the particles at $t = 0$, 1, 2, 3 and 4 s (from the left to right) with $\gamma = 0$ and 0.01 J/m^2, respectively. The bar particles are coloured yellow whilst the chip particles are coloured red. A video is also provided as Supplementary material to show the movement of the particles. As in the previous sections, we first discuss the flow patterns in the original systems (Figs. 26a and 27a). In Fig. 26a, a Y-shape pattern of the chip particles appears at the surface of the bed at $t = 1$ s, i.e., after one revolution. With one more revolution ($t = 2$ s), many chip particles move to the front and the

Y-shape becomes wider. At $t = 3$ s, the particles in the front are mostly the chip particles although small amount of the bar particles can be seen at the centre and sides of the bed. Finally, at $t = 4$ s, more bar particles move to the front at the centre of the bed. In Fig. 27a, many particles are sticking on the mixer wall due to the cohesion force. A V-shape pattern of the chip particles appears in the middle of the bed at $t = 1$ s, which is related to the particles initially sticking on the wall. The flowability of the particles is rather poor, and the angle of repose is larger than that of the cohesionless particles in Fig. 26a which leads to a deeper valley. The SUP model (Figs. 26b–c and 27b–c) can capture both flow patterns described above qualitatively.

Figs. 28 and 29 show the cross-sectional view of the particles at $t = 0$, 1, 2, 3 and 4 s (from the left to right) with $\gamma = 0$ and 0.01 J/m^2, respectively. It is clear that the internal distributions of the bar and chip particles are largely different from those on the front view (Figs. 26 and 27): several layers of the bar and chip particles can be observed after the mixer rotation. It can also be said that the internal distributions of the bar and chip particles are qualitatively similar between the original and scaled-up systems in both the cohesionless and cohesive cases although some of the thin layers cannot be resolved especially with $l = 4$.
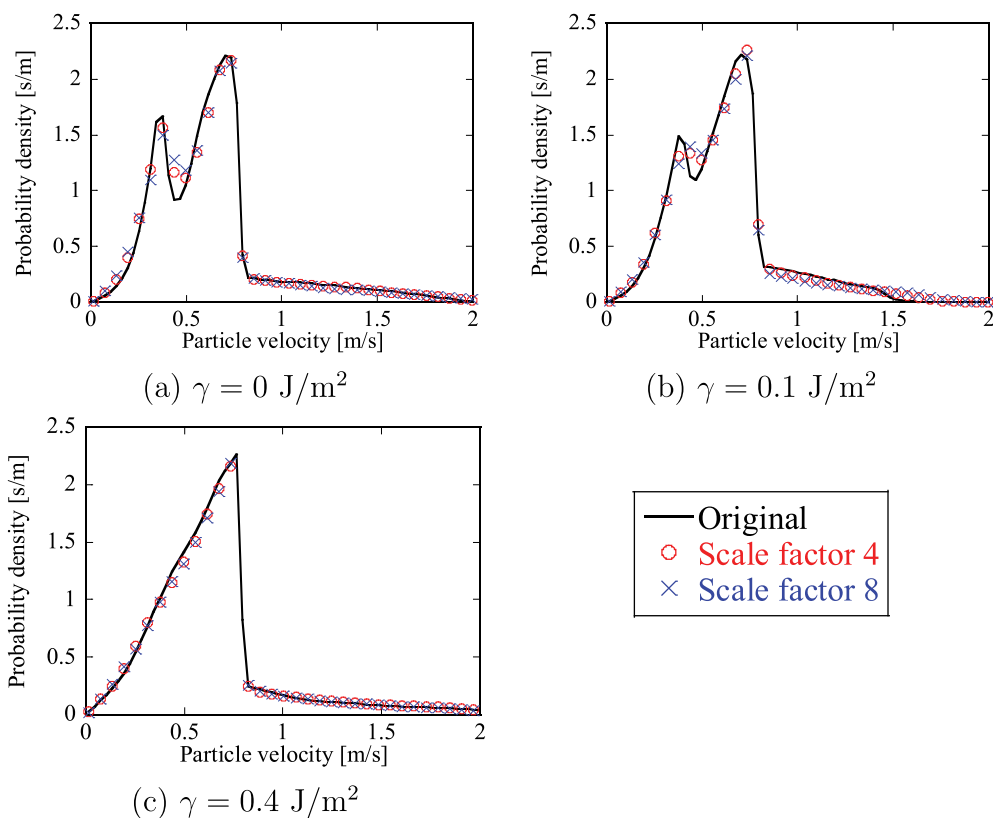
Fig. 24. Probability density distribution of particle velocity in rotary drum with (a) $\gamma = 0$ J/m², (b) $\gamma = 0.1$ J/m² and (c) $\gamma = 0.4$ J/m².
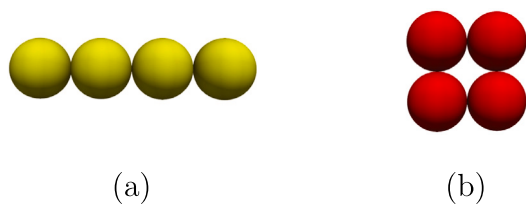

Fig. 25. Shape of particles used for V-mixer; (a) bar and (b) chip. Both of the particles are represented with the multisphere model and consist of 4 identical sub-spheres without overlap.

For more quantitative comparison, the average heights of the bar and chip particles from the rotation axis are plotted in Fig. 30. It can be seen that the fluctuation patterns and the peak values vary with time because of the non-uniformity of the bed. Although the overall frequency and amplitude are somewhat similar between Fig. 30a and b, each peak value is not the same because the cohesion force can affect the particle dynamics and the angle of repose as discussed above. Initially, the heights of the bar and chip particles are significantly different since the particles are almost completely segregated, and the difference becomes smaller as the mixing proceeds. At $t = 4$ s, the heights of the bar and chip particles are roughly the same. The results in the scaled-up systems are in quantitative agreement with those in the original systems regardless of the scale factor. It is concluded that the SUP model can replicate the original flow patterns which fluctuate with time as well as the progression of mixing.

5. Conclusions

In this work, the validity of the Scaled-Up Particle (SUP) model, which is a novel coarse grain model for DEM developed in the authors' previous work [41,43,46], is investigated to simulate a flow of non-spherical and poly-dispersed particles. It is explained that the derivation of the scaling laws in the SUP model is not restricted by particle shape. Therefore, it is inferred that the scaling law can be applied not only to spherical and mono-dispersed particles, as is the case tested in the previous work, but also to non-spherical and poly-dispersed particles without any change in theory. Simulations of a variety of systems are performed to discuss the validity of the model. The key findings in each simulation are summarised below:

- In the compression simulations of packed particle bed, which is a quasi-static and contact force dominant system, it is shown that the SUP model can well replicate the original stress–strain curve using both the superquadric and multisphere models. It is also demonstrated that the l^3 scaling for contact force and torque significantly overestimates the stress.
- In the simulations of heap formation, it is shown that the SUP model can properly capture the effect of various particle shapes in the original system. The bulk volume of the heap obtained from the scaled-up particles is almost identical to that from the original particles regardless of the shape parameters and shape model used. It is also shown that the original bulk volume of a binary mixture (sphere and flat particles) can be well reproduced with the SUP model. This proves that the model can be applied not only to mono-dispersed particles but also poly-dispersed particles.
- Simulations of a high shear mixer are performed to further investigate the validity of the SUP model for dynamic flows of non-spherical and poly-dispersed particles. Both the particle velocity and bed structure can vary with the fraction of different
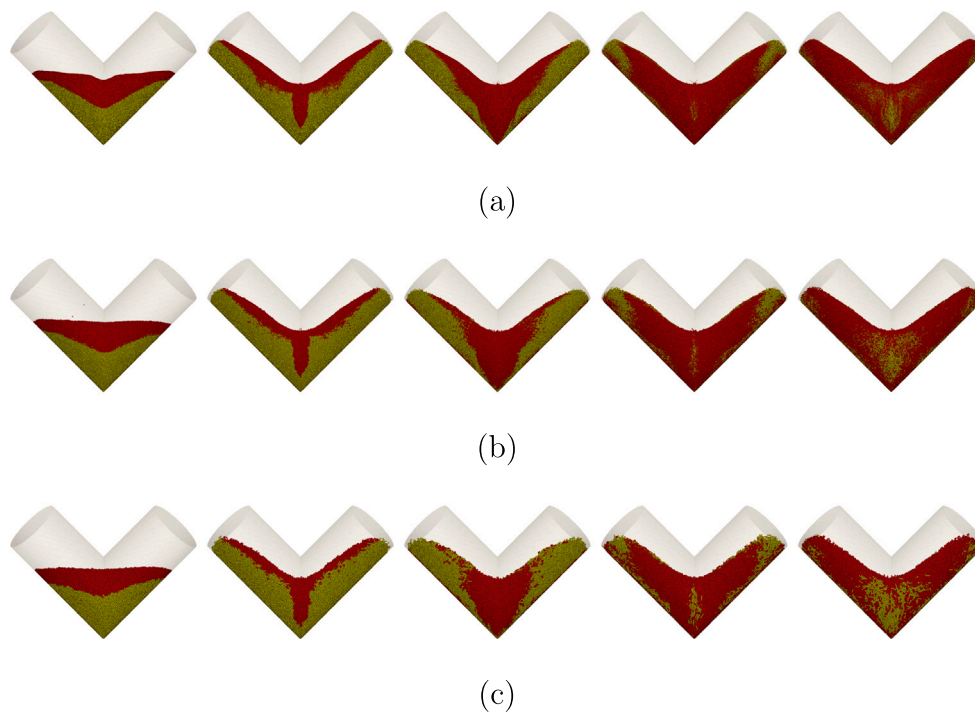
Fig. 26. Front view of the particles in a V-mixer at $t = 0$, 1, 2, 3 and 4 s from left to right with $\gamma = 0$ J/m^2; (a) original, (b) scaled-up ($l = 2$) and (c) scaled-up ($l = 4$) systems. Bar and chip particles are coloured with yellow and red, respectively.
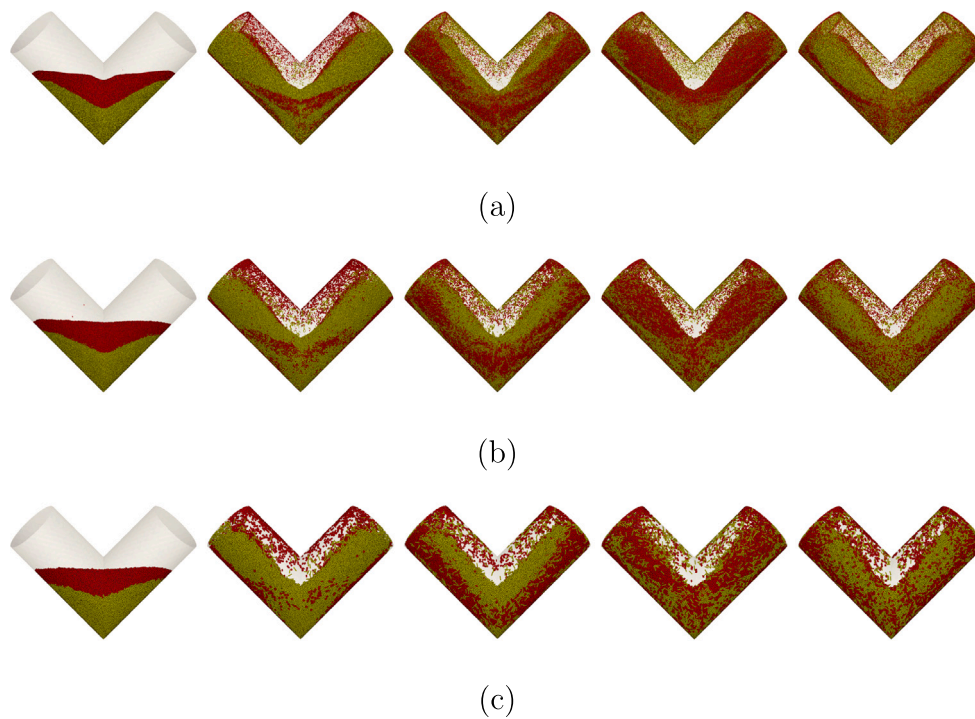

Fig. 27. Front view of the particles in a V-mixer at $t = 0$, 1, 2, 3 and 4 s from left to right with $\gamma = 0.01$ J/m^2; (a) original, (b) scaled-up ($l = 2$) and (c) scaled-up ($l = 4$) systems. Bar and chip particles are coloured with yellow and red, respectively.

shape particles, which can be well replicated with the SUP model. The peak velocity is also compared and a good quantitative agreement can be seen.

• In the simulation of the flow in a large rotary drum, it is shown that the impact of the surface energy on both the overall flow pattern and the flow structure can be well predicted with the SUP
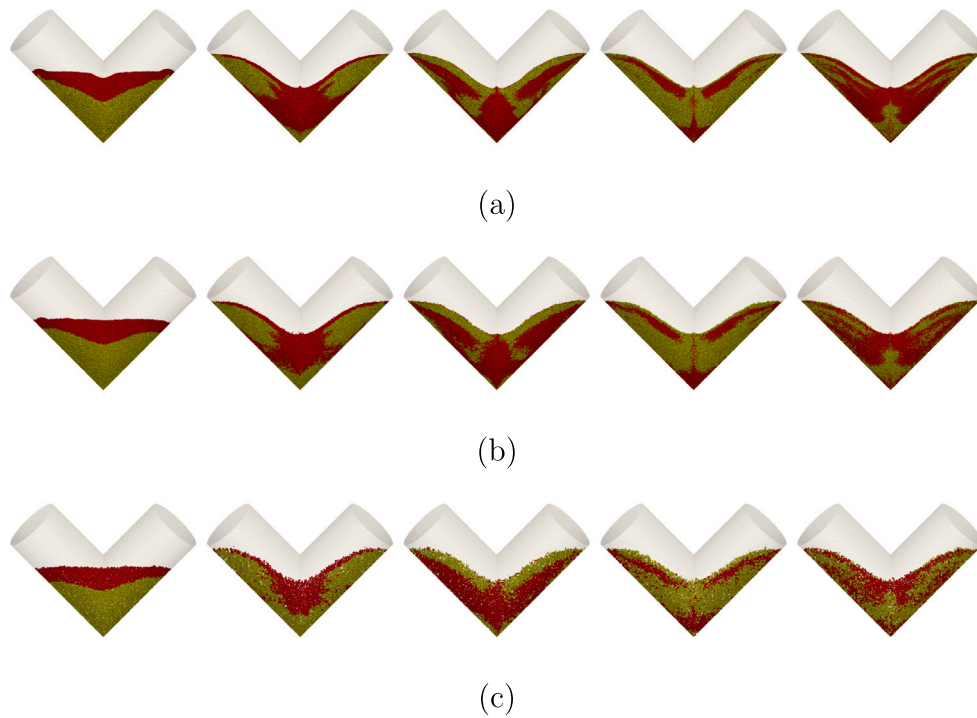
Fig. 28. Cross-sectional view of particles at in a V-mixer at $t = 0$, 1, 2, 3 and 4 s from left to right with $\gamma = 0$ J/m^2; (a) original, (b) scaled-up ($l = 2$) and (c) scaled-up ($l = 4$) systems. Bar and chip particles are coloured with yellow and red, respectively.
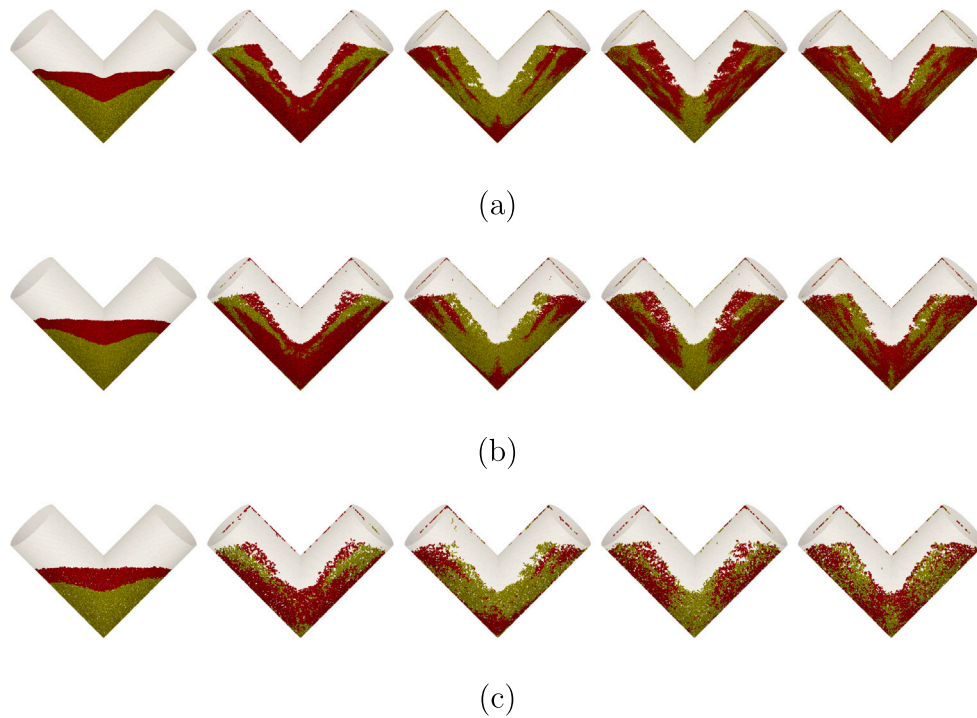

Fig. 29. Cross-sectional view of particles at in a V-mixer at $t = 0$, 1, 2, 3 and 4 s from left to right with $\gamma = 0.01$ J/m^2; (a) original, (b) scaled-up ($l = 2$) and (c) scaled-up ($l = 4$) systems. Bar and chip particles are coloured with yellow and red, respectively.

model. However, some discrepancies from the original system are also observed at larger scale factor. They are caused by the lack of the spacial resolution, i.e., the size of the scaled-up particles is too large to resolve the characteristic flow structure. It is recommended to perform a sensitivity study of the scale factor to ensure that the flow structure of interest is reasonably resolved, which is similar to the sensitivity study one usually performs for CFD simulations.
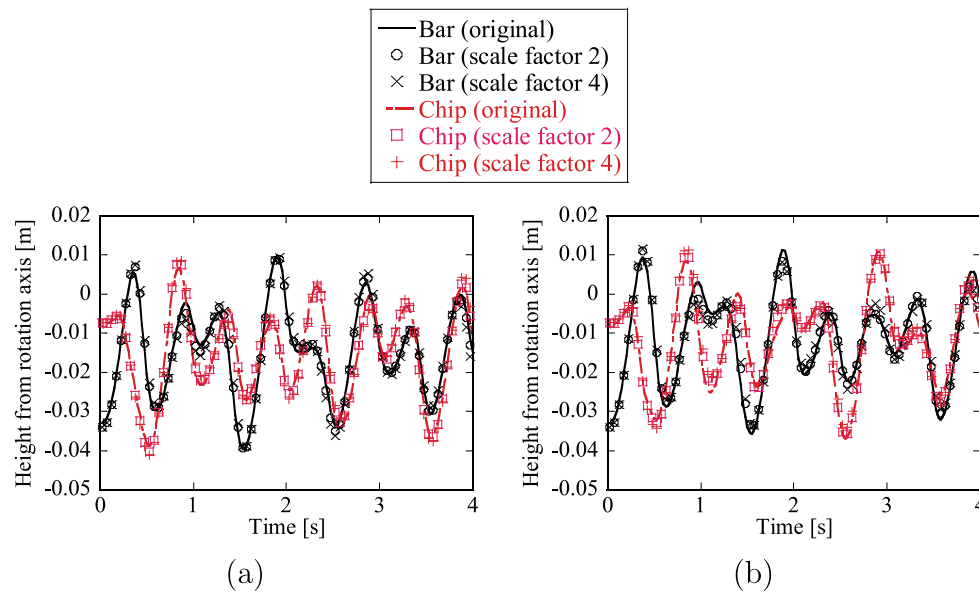
Fig. 30. Average height of particles from rotation axis with (a) $\gamma = 0$ J/m^2 and (b) $\gamma = 0.01$ J/m^2.

- In the simulation of the flow and mixing in a V-mixer, it is shown that the SUP model can reproduce the original flow patterns which can vary with time and the orientation of the equipment. It is also proven that the progression of mixing in the original and scaled-up system is reasonably similar both qualitatively and quantitatively.

CRediT authorship contribution statement

Kimiaki Washino: Conceptualization, Methodology, Software, Validation, Data curation, Investigation, Writing – original draft. **Ei L. Chan:** Validation, Data curation, Software, Investigation, Writing – review & editing. **Yukiko Nishida:** Data curation. **Takuya Tsuji:** Supervision.

Declaration of competing interest

The authors declare that they have no known competing financial interests or personal relationships that could have appeared to influence the work reported in this paper.

Data availability

Data will be made available on request.

Acknowledgements

Appendix A. Supplementary data

Supplementary material related to this article can be found online at https://doi.org/10.1016/j.powtec.2023.118676.

References

[1] P.A. Cundall, O.D.L. Strack, Discrete numerical model for granular assemblies, Geotechnique 29–1 (1979) 47–65, http://dx.doi.org/10.1680/geot.1979.29.1.47.

[2] Y. Tsuji, T. Tanaka, T. Ishida, Lagrangian numerical simulation of plug flow of cohesionless particles in a horizontal pipe, Powder Technol. 71 (1992) 239–250, http://dx.doi.org/10.1016/0032-5910(92)88030-L.

[3] Y. Tsuji, T. Kawaguchi, T. Tanaka, Discrete particle simulation of two-dimensional fluidized bed, Powder Technol. 77 (1993) 79–87, http://dx.doi.org/10.1016/0032-5910(93)85010-7.

[4] K. Iwashita, M. Oda, Rolling resistance at contacts in simulation of shear band development by DEM, J. Eng. Mech. 124 (1998) 285–292, http://dx.doi.org/10.1061/(asce)0733-9399(1998)124:3(285).

[5] J. Ai, J.F. Chen, J.M. Rotter, J.Y. Ooi, Assessment of rolling resistance models in discrete element simulations, Powder Technol. 206 (2011) 269–282, http://dx.doi.org/10.1016/j.powtec.2010.09.030.

[6] P.W. Cleary, DEM prediction of industrial and geophysical particle flows, Particuology 8 (2010) 106–118, http://dx.doi.org/10.1016/j.partic.2009.05.006.

[7] W. Zhong, A. Yu, X. Liu, Z. Tong, H. Zhang, DEM/CFD-DEM modelling of non-spherical particulate systems: Theoretical developments and applications, Powder Technol. 302 (2016) 108–152, http://dx.doi.org/10.1016/j.powtec.2016.07.010, URL https://linkinghub.elsevier.com/retrieve/pii/S0032591016304065.

[8] J. Favier, M. Abbaspour-Fard, M. Kremmer, A. Raji, Shape representation of axi-symmetrical, non-spherical particles in discrete element simulation using multi-element model particles, Eng. Comput. 16 (1999) 467–480, http://dx.doi.org/10.1108/02644409910271894, URL https://www.emerald.com/insight/content/doi/10.1108/02644409910271894/full/html.

[9] H. Kruggel-Emden, S. Rickelt, S. Wirtz, V. Scherer, A study on the validity of the multi-sphere discrete element method, Powder Technol. 188 (2008) 153–165, http://dx.doi.org/10.1016/j.powtec.2008.04.037, URL https://linkinghub.elsevier.com/retrieve/pii/S0032591008002143.

[10] D. Markauskas, R. Kačianauskas, A. Džiugys, R. Navakas, Investigation of adequacy of multi-sphere approximation of elliptical particles for DEM simulations, Granul. Matter 12 (2010) 107–123, http://dx.doi.org/10.1007/s10035-009-0158-y.

[11] B. Soltanbeigi, A. Podlozhnyuk, S.A. Papanicolopulos, C. Kloss, S. Pirker, J.Y. Ooi, DEM study of mechanical characteristics of multi-spherical and superquadric particles at micro and macro scales, Powder Technol. 329 (2018) 288–303, http://dx.doi.org/10.1016/J.POWTEC.2018.01.082.

[12] B. Kravets, D. Schulz, R. Jasevičius, S.R. Reinecke, T. Rosemann, H. Kruggel-Emden, Comparison of particle-resolved DNS (PR-DNS) and non-resolved DEM/CFD simulations of flow through homogenous ensembles of fixed spherical and non-spherical particles, Adv. Powder Technol. 32 (2021) 1170–1195, http://dx.doi.org/10.1016/j.apt.2021.02.016.

[13] P. Cundall, Formulation of a three-dimensional distinct element model—Part I. A scheme to detect and represent contacts in a system composed of many polyhedral blocks, Int. J. Rock Mech. Min. Sci. Geomech. Abstr. 25 (1988) 107–116, http://dx.doi.org/10.1016/0148-9062(88)92293-0.

[14] S.-W. Chang, C.-S. Chen, A non-iterative derivation of the common plane for contact detection of polyhedral blocks, Internat. J. Numer. Methods Engrg. 74 (2008) 734–753, http://dx.doi.org/10.1002/nme.2174.

[15] C. Boon, G. Houlsby, S. Utili, A new algorithm for contact detection between convex polygonal and polyhedral particles in the discrete element method, Comput. Geotech. 44 (2012) 73–82, http://dx.doi.org/10.1016/j.compgeo.2012.03.012.

[16] Barr, Superquadrics and angle-preserving transformations, IEEE Comput. Graph. Appl. 1 (1981) 11–23, http://dx.doi.org/10.1109/MCG.1981.1673799.

[17] J.R. Williams, A.P. Pentland, Superquadrics and modal dynamics for discrete elements in interactive design, Eng. Comput. 9 (1992) 115–127, http://dx.doi.org/10.1108/eb023852.

[18] P.W. Cleary, M.L. Sawley, DEM modelling of industrial granular flows: 3D case studies and the effect of particle shape on hopper discharge, Appl. Math. Model. 26 (2002) 89–111, http://dx.doi.org/10.1016/S0307-904X(01)00050-6.

[19] N. Govender, D.N. Wilke, C.Y. Wu, R. Rajamani, J. Khinast, B.J. Glasser, Large-scale GPU based DEM modeling of mixing using irregularly shaped particles, Adv. Powder Technol. 29 (2018) 2476–2490, http://dx.doi.org/10.1016/j.apt.2018.06.028.

[20] Y. He, T.J. Evans, A.B. Yu, R.Y. Yang, A GPU-based DEM for modelling large scale powder compaction with wide size distributions, Powder Technol. 333 (2018) 219–228, http://dx.doi.org/10.1016/j.powtec.2018.04.034.

[21] Y. He, F. Muller, A. Hassanpour, A.E. Bayly, A CPU-GPU cross-platform coupled CFD-DEM approach for complex particle-fluid flows, Chem. Eng. Sci. 223 (2020) 115712, http://dx.doi.org/10.1016/j.ces.2020.115712.

[22] T. Tsuji, K. Yabumoto, T. Tanaka, Spontaneous structures in three-dimensional bubbling gas-fluidized bed by parallel DEM-CFD coupling simulation, Powder Technol. 184 (2008) 132–140, http://dx.doi.org/10.1016/j.powtec.2007.11.042, cited By 92.

[23] H. Mio, R. Higuchi, W. Ishimaru, A. Shimosaka, Y. Shirakawa, J. Hidaka, Effect of paddle rotational speed on particle mixing behavior in electrophotographic system by using parallel discrete element method, Adv. Powder Technol. 20 (2009) 406–415, http://dx.doi.org/10.1016/j.apt.2009.05.002.

[24] J. Hærvig, U. Kleinhans, C. Wieland, H. Spliethoff, A.L. Jensen, K. Sørensen, T.J. Condra, On the adhesive JKR contact and rolling models for reduced particle stiffness discrete element simulations, Powder Technol. 319 (2017) 472–482, http://dx.doi.org/10.1016/j.powtec.2017.07.006.

[25] T. Kobayashi, T. Tanaka, N. Shimada, T. Kawaguchi, DEM-CFD analysis of fluidization behavior of Geldart Group A particles using a dynamic adhesion force model, Powder Technol. 248 (2013) 143–152, http://dx.doi.org/10.1016/j.powtec.2013.02.028.

[26] K. Washino, E.L. Chan, T. Tanaka, DEM with attraction forces using reduced particle stiffness, Powder Technol. 325 (2018) 202–208, http://dx.doi.org/10.1016/j.powtec.2017.11.024.

[27] S. Chen, W. Liu, S. Li, A fast adhesive discrete element method for random packings of fine particles, Chem. Eng. Sci. 193 (2019) 336–345, http://dx.doi.org/10.1016/j.ces.2018.09.026.

[28] Y. He, A. Hassanpour, M.A. Behjani, A.E. Bayly, A novel stiffness scaling methodology for discrete element modelling of cohesive fine powders, Appl. Math. Model. 90 (2021) 817–844, http://dx.doi.org/10.1016/j.apm.2020.08.062.

[29] M. Sakai, S. Koshizuka, Large-scale discrete element modeling in pneumatic conveying, Chem. Eng. Sci. 64 (2009) 533–539, http://dx.doi.org/10.1016/j.ces.2008.10.003.

[30] C. Bierwisch, T. Kraft, H. Riedel, M. Moseler, Three-dimensional discrete element models for the granular statics and dynamics of powders in cavity filling, J. Mech. Phys. Solids 57 (2009) 10–31.

[31] M. Sakai, H. Takahashi, C.C. Pain, J.P. Latham, J. Xiang, Study on a large-scale discrete element model for fine particles in a fluidized bed, Adv. Powder Technol. 23 (2012) 673–681, http://dx.doi.org/10.1016/j.apt.2011.08.006.

[32] M. Sakai, M. Abe, Y. Shigeto, S. Mizutani, H. Takahashi, A. Viré, J.R. Percival, J. Xiang, C.C. Pain, Verification and validation of a coarse grain model of the DEM in a bubbling fluidized bed, Chem. Eng. J. 244 (2014) 33–43, http://dx.doi.org/10.1016/j.cej.2014.01.029.

[33] S.C. Thakur, J.Y. Ooi, H. Ahmadian, Scaling of discrete element model parameters for cohesionless and cohesive solid, Powder Technol. 293 (2016) 130–137.

[34] K. Takabatake, Y. Mori, J.G. Khinast, M. Sakai, Numerical investigation of a coarse-grain discrete element method in solid mixing in a spouted bed, Chem. Eng. J. 346 (2018) 416–426, http://dx.doi.org/10.1016/j.cej.2018.04.015.

[35] P.M. Widartiningsih, Y. Mori, K. Takabatake, C.Y. Wu, K. Yokoi, A. Yamaguchi, M. Sakai, Coarse graining DEM simulations of a powder die-filling system, Powder Technol. 371 (2020) 83–95, http://dx.doi.org/10.1016/j.powtec.2020.05.063.

[36] Z. Xie, Y. Shen, K. Takabatake, A. Yamaguchi, M. Sakai, Coarse-grained DEM study of solids sedimentation in water, Powder Technol. 361 (2020) 21–32, http://dx.doi.org/10.1016/j.powtec.2019.11.034.

[37] Y. Mori, M. Sakai, Visualization study on the coarse graining DEM for large-scale gas–solid flow systems, Particuology 59 (2021) 24–33, http://dx.doi.org/10.1016/j.partic.2020.07.001, URL https://linkinghub.elsevier.com/retrieve/pii/S1674200120300791.

[38] Z. Jiang, K. Rai, T. Tsuji, K. Washino, T. Tanaka, J. Oshitani, Upscaled DEM-CFD model for vibrated fluidized bed based on particle-scale similarities, Adv. Powder Technol. 31 (2020) 4598–4618, http://dx.doi.org/10.1016/j.apt.2020.10.009.

[39] H. Nakamura, H. Takimoto, N. Kishida, S. Ohsaki, S. Watano, Coarse-grained discrete element method for granular shear flow, Chem. Eng. J. Adv. 4 (2020) http://dx.doi.org/10.1016/J.CEJA.2020.100050.

[40] M.J. de Munck, J.B. van Gelder, E.A. Peters, J.A. Kuipers, A detailed gas-solid fluidized bed comparison study on CFD-DEM coarse-graining techniques, Chem. Eng. Sci. 269 (2023) http://dx.doi.org/10.1016/j.ces.2022.118441.

[41] Y. Hu, E.L. Chan, T. Tsuji, T. Tanaka, K. Washino, Geometric similarity on interparticle force evaluation for scaled-up DEM particles, Powder Technol. 404 (2022) 117483, http://dx.doi.org/10.1016/j.powtec.2022.117483, URL https://linkinghub.elsevier.com/retrieve/pii/S0032591022003771.

[42] A.D. Renzo, E. Napolitano, F.D. Maio, Coarse-grain DEM modelling in fluidized bed simulation: A review, Processes 9 (2021) 279, http://dx.doi.org/10.3390/pr9020279, URL https://www.mdpi.com/2227-9717/9/2/279.

[43] E.L. Chan, K. Washino, Coarse grain model for DEM simulation of dense and dynamic particle flow with liquid bridge forces, Chem. Eng. Res. Des. 132 (2018) 1060–1069, http://dx.doi.org/10.1016/j.cherd.2017.12.033.

[44] K. Chu, J. Chen, A. Yu, Applicability of a coarse-grained CFD–DEM model on dense medium cyclone, Miner. Eng. 90 (2016) 43–54, http://dx.doi.org/10.1016/j.mineng.2016.01.020.

[45] K. Chu, Y. Chen, L. Ji, Z. Zhou, A. Yu, J. Chen, Coarse-grained CFD-DEM study of gas-solid flow in gas cyclone, Chem. Eng. Sci. 260 (2022) http://dx.doi.org/10.1016/j.ces.2022.117906.

[46] K. Washino, E.L. Chan, T. Kaji, Y. Matsuno, T. Tanaka, On large scale CFD–DEM simulation for gas–liquid–solid three-phase flows, Particuology 59 (2021) 2–15, http://dx.doi.org/10.1016/j.partic.2020.05.006, URL https://linkinghub.elsevier.com/retrieve/pii/S1674200120300754.

[47] C. Kloss, C. Goniva, A. Hager, S. Amberger, S. Pirker, Models, algorithms and validation for opensource DEM and CFD-DEM, Prog. Comput. Fluid Dyn. 12 (2012) 140–152, http://dx.doi.org/10.1504/PCFD.2012.047457.

[48] W.R. Hamilton, LXIX. <i>On quaternions; or on a new system of imaginaries in algebra</i>, Lond. Edinb. Dublin Philos. Mag. J. Sci. 30 (1847) 458–461, http://dx.doi.org/10.1080/14786444708645426, URL https://www.tandfonline.com/doi/full/10.1080/14786444708645426.

[49] K.L. Johnson, K. Kendal, A.D. Roberts, Surface energy and the contact of elastic solids, Proc. R. Soc. Lond. Ser. A Math. Phys. Eng. Sci. 324 (1971) 301–313, http://dx.doi.org/10.1098/rspa.1971.0141.

[50] E.J. Parteli, J. Schmidt, C. Blümel, K.E. Wirth, W. Peukert, T. Pöschel, Attractive particle interaction forces and packing density of fine glass powders, Sci. Rep. 4 (2014) 1–7, http://dx.doi.org/10.1038/srep06227.

[51] C. Thornton, Interparticle sliding in the presence of adhesion, J. Phys. D: Appl. Phys. 24 (1991) 1942–1946, http://dx.doi.org/10.1088/0022-3727/24/11/007.

[52] J.S. Marshall, Discrete-element modeling of particulate aerosol flows, J. Comput. Phys. 228 (2009) 1541–1561, http://dx.doi.org/10.1016/j.jcp.2008.10.035.

[53] A. Podlozhnyuk, S. Pirker, C. Kloss, Efficient implementation of superquadric particles in discrete element method within an open-source framework, Comput. Part. Mech. 4 (2017) 101–118, http://dx.doi.org/10.1007/s40571-016-0131-6.

[54] R.B. Bird, W.E. Stewart, E.N. Lightfoot, Transport Phenomena, second ed., New York, Wiley, 2002.

[55] M. Alizadeh, A. Hassanpour, M. Pasha, M. Ghadiri, A. Bayly, The effect of particle shape on predicted segregation in binary powder mixtures, Powder Technol. 319 (2017) 313–322, http://dx.doi.org/10.1016/j.powtec.2017.06.059.

[56] A.A. Boateng, P.V. Barr, Modelling of particle mixing and segregation in the transverse plane of a rotary kiln, Chem. Eng. Sci. 51 (1996) 4167–4181, http://dx.doi.org/10.1016/0009-2509(96)00250-3.

[57] A.J. Morrison, I. Govender, A.N. Mainza, D.J. Parker, The shape and behaviour of a granular bed in a rotating drum using Eulerian flow fields obtained from PEPT, Chem. Eng. Sci. 152 (2016) 186–198, http://dx.doi.org/10.1016/j.ces.2016.06.022.

[58] H.P. Kuo, P.C. Knight, D.J. Parker, Y. Tsuji, M.J. Adams, J.P. Seville, The influence of DEM simulation parameters on the particle behaviour in a V-mixer, Chem. Eng. Sci. 57 (2002) 3621–3638, http://dx.doi.org/10.1016/S0009-2509(02)00086-6.